IAS SEDIMENTOLOGY
Journal of the International Association of Sedimentologists

# Depositional Processes, Bedform Development and Hybrid Bed Formation in Rapidly Decelerated Cohesive (Mud-Sand) Sediment Flows



| | |
|---|---|
| Journal: | *Sedimentology* |
| Manuscript ID: | SED-2010-OM-137.R1 |
| Manuscript Type: | Original Manuscript |
| Keywords: | Bedforms, Current ripples, Decelerating flows, Turbulence modulation, Bed shear strength, Cohesion, Clay suspensions, Hybrid beds |
| | |

# Depositional Processes, Bedform Development and Hybrid Bed Formation in Rapidly Decelerated Cohesive (Mud-Sand) Sediment Flows

**JACO H. BAAS[1], JAMES L. BEST[2] & JEFFREY PEAKALL[3]**

*[1]School of Ocean Sciences, Bangor University, Menai Bridge LL59 5AB, Wales, United Kingdom*

*[2]Departments of Geology, Geography and Mechanical Science and Engineering and Ven Te Chow Hydrosystems Laboratory, University of Illinois at Urbana-Champaign, 1301 West Green Street, Urbana, Illinois 61801, U.S.A.*

*[3]School of Earth and Environment, University of Leeds, Woodhouse Lane, Leeds LS2 9JT, United Kingdom*

Running title*: Bedforms in decelerated cohesive flows*

*Keywords*: Bedforms; Current ripples; Flow deceleration; Turbulence modulation; Bed shear strength; Cohesion; Clay suspensions; Hydrid beds

## ABSTRACT

Flows with high suspended sediment concentrations are common in many sedimentary environments, and their flow properties may show a transitional behaviour between fully turbulent and quasi-laminar plug flows. The characteristics of these transitional flows are a function of both clay concentration and type as well as the applied fluid stress. This paper investigates the behaviour of rapidly decelerated to steady flows that contain a mixture of sand, silt and clay, and explores the effect of different clay (kaolin) concentrations on the dynamics of flow over a mobile bed, and the bedforms and stratification produced. Experiments were conducted in a recirculating slurry flume capable of transporting high clay concentrations. Ultrasonic Doppler velocity profiling was used to measure the flow velocity within these concentrated suspension flows. The development of current ripples under decelerated flows of differing kaolin concentration was documented and evolution of their height, wavelength and migration rate quantified.

This work confirms past work over smooth, fixed beds, which showed that, as clay concentration rises, a distinct sequence of flow types is generated: turbulent flow (TF), turbulence-enhanced transitional flow (TETF), lower transitional plug flow (LTPF), upper transitional plug flow (UTPF) and a quasi-laminar plug flow (QLPF). Each of these flow types produces an initial flat bed upon rapid flow deceleration, followed by reworking of these deposits through the development of current ripples during the subsequent steady flow in TF, TETF and LTPF. The initial flat beds are structureless, but have diagnostic textural properties, caused by differential settling of sand, silt and cohesive mud, which forms characteristic bipartite beds that initially consist of sand overlain by silt or clay. As clay concentration in the formative flow increases, ripples first increase in mean height and wavelength under TETF and LTPF regimes, which is attributed to the additional turbulence generated under these flows that subsequently causes greater leeside erosion. As clay concentration increases further from a LTPF, ripples cease to exist under the UTPF and QLPF conditions investigated herein. This disappearance of ripples appears due to both turbulence suppression at higher clay concentrations, as well as the increasing shear strength of the bed sediment that becomes more difficult to erode as clay concentration increases. The stratification within the ripples formed after rapid deceleration of the transitional flows reflects the availability of sediment from the bipartite bed. The exact nature of the ripple cross-stratification in these flows is a direct function of the duration of the formative flow and the texture of the initial flat bed, and ripples do not to form in cohesive flows with a Reynolds number smaller than ~12,000.

Examples are given of how the unique properties of the current ripples and plane beds, developing below decelerated transitional flows, could aid in the interpretation of depositional processes in modern and ancient sediments. This includes a new model for hybrid beds that explains their formation in terms of a combination of vertical grain-size segregation and longitudinal flow transformation.

## 1. INTRODUCTION

Sediment-laden flows of high density occur in most natural environments, and their depositional products may comprise a significant part of the sedimentary rock record. For instance, river channels may form the conduit of subaerial debris flows and hyperconcentrated flows, especially in mountainous regions where large volumes of weathered sediment are available (e.g. Van Maren *et al.*, 2009), whilst lahars are dense, and highly destructive, mixtures of sediment and water that move down the slopes of volcanoes (Pierson, 1985; Best, 1992). During storms combined with high rainfall in shallow marine environments, large quantities of sediment may be flushed out of estuaries onto the continental shelf by means of mobile fluid muds (e.g. “oceanic floods” of Traykovski *et al.* 2000). Flows of high density are probably most common on the continental slope and continental rise, where a large variety of sediment gravity flow deposits has been found in submarine fans, both in contemporary environments and in the geological record (e.g. Dasgupta, 2003). These deposits include turbidites, submarine debris flow deposits, slurry flow deposits, linked debrites-turbidites (i.e. hybrid event beds), and submarine slump and slide deposits (e.g. Mulder & Alexander, 2001; Haughton *et al.*, 2009). Despite their common occurrence, the interaction of high-density flows with their substrate and the formation of any diagnostic sedimentary structures are still poorly understood when compared to low-density flows. This is partly because only since the introduction of ultrasonic Doppler velocimetry profiling (Best *et al.*, 2001; Baas & Best, 2002) has it become possible to reveal the complex internal dynamics of flows in laboratory experiments that transport large amounts of sand, silt and clay.

The dynamics of high-density flows are unique, and recent work has shown that clearwater or low-density flows cannot be used as a surrogate for high-density flows (Mulder & Alexander, 2001; Baas & Best, 2002; Baas *et al.*, 2009), especially if these flows transport clay particles. Clay has cohesive properties, because electrostatic forces cause the particles to attract each other, thus forming clay flocs or gels (i.e., pervasive, volume-filling networks of bonded clay particles). These particle bonds can make a flow strong enough to modulate turbulence, or, if turbulent enough, a flow can break relatively weak clay flocs or clay gels into smaller constituents. This feedback between clay concentration and applied fluid stress controls not only the flow properties, but may also affect the exchange of sediment between bed and flow, and thus may be expected to have important implications for depositional properties. The present paper compares the depositional properties of low- and high-density flows by investigating the development of bedforms and their sedimentary structures across a wide range of suspended sediment concentrations, including turbulent, transitional and quasi-laminar flow phases (*sensu* Baas *et al.*, 2009). This approach is inspired by the fact that bedform analysis is an essential tool for modelling sediment transport in modern environments and reconstructing sedimentary processes from core and outcrop data.

Natural high-density flows often lose their sediment load quickly when the driving force is removed, such as by a reduction in slope angle or decrease in flow confinement. This may give rise to characteristic deposit shapes, such as the blunt frontal terminations of debris flow deposits

(Amy *et al.*, 2005; Amy & Talling, 2006), and characteristic internal organisation, such as massive, "structureless", sandstones (Stow & Johansson, 2000). In the present laboratory experiments, conditions of rapid depletion were simulated using open-channel suspension flows that were supersaturated with sediment and thus highly depositional. This produced unique bedforms, the form and size of which varied greatly, yet in a predictable manner, with suspended clay concentration. These geometrical variations were governed by processes of turbulence modulation and by differential settling of non-cohesive sand, silt and cohesive mud.

## 2. TURBULENT, TRANSITIONAL AND QUASI-LAMINAR FLOWS

Turbulence modulation in a flow laden with clay particles is dependent on the properties of both the fluid and the boundary over which the flow is moving. The properties of a turbulent flow may change as a function of fluid shear, clay type and clay concentration (i.e. viscosity and yield strength), bed surface roughness (including grain and bedform roughness) and distance from the sediment bed. The complex interaction of these parameters renders predictions of turbulence modulation a difficult task, and past experimental work has therefore taken a stepwise approach by investigating each parameter in isolation. Baas & Best (2002) and Baas *et al.* (2009) studied the flow of kaolin-laden fluids over a smooth, fixed, horizontal bed and revealed a distinct series of changes in the properties of turbulent flow as clay concentration and mean flow velocity were increased. Other laboratory experiments have focussed on the influence of grain roughness, by comparing the mean and turbulent flow properties of clay-rich flows moving over a smooth and rough (7 mm gravel) surface (Baas & Best, 2009), and on form drag in flows over a fixed, idealised current ripple (Baas & Best, 2008).

Baas *et al.* (2009) proposed a clay-flow phase diagram with five flow-phase stability fields (Fig. 1). At the lowest suspended clay concentrations, a normal turbulent flow (TF) is present, with a standard logarithmic velocity profile and turbulence intensities that decrease away from the bed (Fig. 2). In the TF phase, turbulent fluctuations in flow velocity were inferred to be strong enough to prevent the clay from forming cohesive bonds, and the flow dynamics were similar to clearwater flows. At the highest clay concentrations, however, the clay particles formed a pervasive gel, making the flow viscous and suppressing most of the turbulence. This 'quasi-laminar plug flow' (QLPF) is characterised by a rigid plug without internal deformation, i.e. the yield strength exceeds the shear stresses within the plug. The rigid plug moves on top of a weakly turbulent to laminar basal shear layer (Fig. 2). Between these two extremes, three types of 'transitional flow' were distinguished; with increasing clay concentration: turbulence-enhanced transitional flow (TETF); lower transitional plug flow (LTPF); and upper transitional plug flow (UTPF) (Fig. 1). TETF is characterised by enhanced turbulence intensity over the entire flow depth, with an internal shear layer just above the bed being inferred to be the source of this additional turbulence (Baas and

Best, 2002; Baas *et al.*, 2009). This shear layer separates a lower, thickened viscous sublayer from the overriding flow. Vorticity, in the form of Kelvin-Helmholtz instabilities, penetrates upwards into the flow from the shear layer, whilst gradually dissipating (Fig. 2; Baas and Best, 2002). LTPF forms at higher clay concentrations than TETF, and is characterised by the formation of a plug flow region, which is virtually free of turbulence and has low, or no, vertical gradients in downstream velocity (Fig. 2). The plug flow forms first near the water surface, where shear is lowest, and expands downward as clay concentration is increased. However, turbulence enhancement, probably by the same process as in the TETF, persists near the bed in LTPF, thus maximising the gradient of turbulent intensity between the base and top of the flow (Fig. 2). At around the height of the internal shear layer in LTPF, the velocity time-series contains saw-tooth shaped velocity fluctuations with a periodicity of up to 10 s, which were also interpreted to be caused by Kelvin-Helmholtz instabilities (Fig. 2; Baas and Best, 2002; Baas *et al.*, 2009). UTPF is a flow intermediate between LTPF and QLPF (Fig. 1), in which the plug flow region thickens as clay concentration increases, whilst turbulence is attenuated along the entire flow depth, as turbulence forces are progressively outbalanced by viscosity and yield strength (i.e. cohesive forces) of the suspended clay (Fig. 2). Although the basal shear layer still exists in UTPF, it becomes a progressively weaker source of turbulence, until it ceases to produce turbulence altogether in QLPF.

Baas & Best (2008) extended the work of Baas & Best (2002) by introducing kaolin-laden flows over a smooth, idealised, fixed current ripple, and investigated the dynamics of turbulent, transitional and laminar flow above and downstream of the ripple crest. With increasing suspended clay concentration, Baas & Best (2008) identified the following principal flow types: (1) Normal turbulent flow, dominated by flow separation downstream of the ripple crest; (2) Turbulence-enhanced transitional flow, which is analogous to the TETF and LTPF of Baas *et al.* (2009) (phase 1 in Fig. 3), with increased turbulence intensities along the free shear layer of the separation zone, within the separation zone and at flow reattachment, and generally low turbulence levels in the free flow above the ripple due to the initial development of a plug flow; (3) Turbulence-attenuated transitional flows (phases 2 and 3 in Fig. 3, analogous to the UTPF of Baas *et al.*, 2009), in which strong cohesive forces dampen fluid turbulence within the entire separation zone and a thick plug flow develops in the free flow above the ripple; and (4) Laminar flow with full gelling, (Phase 4 in Fig. 3), which is characterised by the presence of a pronounced laminar plug flow, analogous to the QLPF of Baas *et al.* (2009), with a region of stagnant flow in the ripple lee. Furthermore, Baas & Best (2008) distinguished two phases of turbulence-attenuated transitional flow. At Phase-2 clay concentrations (Fig. 3), turbulence is attenuated within the separation zone, but the length of the separation zone is similar to that under turbulent flow and turbulence-enhanced transitional flows. However, in the highly concentrated turbulence-attenuated transitional flow (Phase 3 in Fig. 3), the separation zone shortens in length, and is associated with a further decrease in turbulence intensity. Baas & Best (2008) reasoned that the spatially-variable nature of turbulence production

over a bedform influenced how the interactions between cohesive and turbulence forces affected the structure of clay flows at different locations across the ripple profile. Since the production of turbulence at the base of the ripple lee slope is low, Baas & Best (2008) argued that a stable gel thus forms at a lower clay concentration than in the free shear layer of the separation zone, where strong mixing occurs, and at flow reattachment, where instantaneous bed shear stresses are higher than anywhere else in the ripple trough. It can be hypothesised that these spatial differences in turbulence modulation will have important implications for the development and stability of bedforms in mobile sediment, and thus provide a potential mechanism for differences in bedform shape and size formed in transitional clay flows.

Furthermore, the process of near-bed turbulence enhancement in the ripple lee increases the potential for bed erosion, and may therefore lead to an increase in the development rate and equilibrium size of natural bedforms (Baas & Best, 2008). Conversely, near-bed turbulence attenuation may reduce the potential for bed erosion, and cause bedforms to develop more slowly, and their equilibrium size to be smaller, than in turbulent flow. However, these speculations concerning transitional flow bedforms must be treated with caution, since the experiments of Baas & Best (2008) were limited in that they did not investigate mobile bedforms and hence were unable to erode the bed. Consequently, the possible effect of the infiltration of fine-grained material into the bed upon the mechanical properties of the bed (Packman & MacKay, 2003) and bedform development were not investigated.

The new experimental results presented herein address these previous simplifications and analyse the formation of bedforms in mobile sediment, thus investigating another important variable that must be considered when developing more accurate predictions of the feedback mechanisms between sediment beds and both transitional and laminar clay flows in natural environments. It should be emphasised that the present experiments detail the formation of bedforms below rapidly decelerated open-channel flows laden with a mixture of sand, silt and clay, in which cohesive forces in the flows were at least as important as cohesive forces within the actively-forming sediment bed. This is in contrast to conditions that start with clear water and mixed sand-clay beds, in which bed cohesion may be expected to have the largest impact on bedform dynamics.

## 3. EXPERIMENTAL SETUP AND METHODOLOGY

Fourteen laboratory experiments were conducted using an 8.75 m long and 0.3 m wide slurry flume in the Sorby Environmental Fluid Dynamics Laboratory, University of Leeds (Table 1; Fig. 4). A range of mixtures of fresh water, cohesive clay and non-cohesive silt and sand were circulated through the flume by means of a variable-discharge slurry pump with an open, centrifugal screw mechanism (Fig. 4) that produced minimal flow disturbance. The exception was Run 1, which was

a control experiment with non-cohesive sediment only. The cohesive clay used in the experiments was kaolin with a median diameter, $D_{50}$, of 0.0073 mm, whilst the non-cohesive sediment had a bimodal grain-size distribution with a median diameter of 0.084 mm and modal sizes of 0.048 mm and 0.300 mm (Fig. 5). At the upstream end of the flume, in order to straighten flow at the inlet and dampen any inlet turbulence, all flows moved underneath a wooden board set flush with the water surface, through a grid and then through a horizontal stack of pipes (Fig. 4). Downstream of the pipe stack, the flows moved over a fixed bed of medium-sized gravel along the entire length of the flume. The mean roughness height of the gravel bed was ~8 mm. Turbulence production over the gravel bed was sufficient to keep most sand, silt and clay particles in suspension at high flow discharge (~50 L $s^{-1}$, equivalent to a mean flow velocity of 1.2 m $s^{-1}$), and thus allowed simulation of a steady-state suspension flow at the start of each experiment. At the start of each run, once the flows had been recirculated at 50 L $s^{-1}$ for several minutes, the discharge was reduced instantaneously to ~19 L $s^{-1}$ (equivalent to a flow velocity of ~0.46 m $s^{-1}$ at a flow depth of 0.15 m), thus producing a supersaturated suspension load. The sediment that was deposited from the suspension formed a horizontal bed on which bedform development could take place. This sediment settled quickly and covered the gravel surface so that the underlying gravel clasts did not influence subsequent bedform development in the sand-silt-clay mixture.

The development of the bed was monitored through the sidewall of the flume using digital photographs, line drawings and detailed descriptions of the sedimentological properties of the bed. The height and wavelength of the bedforms was tracked, with each individual bedform being numbered to allow calculation of bedform migration rates. Ultrasonic Doppler velocimetry profiling (UDVP; Best *et al.*, 2001; Baas and Best, 2002, 2008) was used to measure the downstream component of flow velocity at seven or more different heights above the sediment bed near the end of each run. Additional velocity time-series were collected at the start and middle of selected runs. UDVP quantifies flow velocity by determining the Doppler shift in ultrasound frequency as small particles pass through a measurement volume; these probes are particularly well-suited for measuring velocities in opaque suspensions (Takeda, 1991; Best *et al.*, 2001; Baas and Best, 2002). The present experiments used 4 MHz UDVP probes, of 8 mm diameter that acquired simultaneous velocity data along a profile of up to 128 points along the axis of the ultrasound beam, which in the present experiments extended up to 0.105 m from the probe head. No velocities were recorded in the proximal 0.012 m of each profile, where the stagnation of flow by the probes was found to be unacceptably large. The UDVP probes collected velocity data for a duration of 75-87 s at a temporal resolution of 115-133 Hz.

The temporal mean flow velocity, $\overline{U}$ , and its root-mean square, *RMS(u'),* which approximates the horizontal component of turbulence intensity, were calculated from the time-series of instantaneous velocity data at each measurement location:

$$\overline{U} = \frac{1}{n}\sum_{i=1}^{n} u_i$$
$$RMS(u') = \sqrt{\frac{1}{n}\sum_{i=1}^{n}(u_i - \overline{U})^2} \quad (1)$$

where *n* is the number of velocity measurements. For turbulent and low-density transitional flows, the depth-averaged flow velocity, $\overline{\overline{U}}$, was computed using a curve-fitting procedure based on the logarithmic law for wall-bounded shear flows (e.g. Van Rijn, 1990):

$$\overline{\overline{U}} = \frac{1}{h - z_0}\int_{z_0}^{h} \frac{u_*}{\kappa}\ln\left(\frac{z}{z_0}\right) dz \quad (2)$$

where $u_*$ is the shear velocity, $\kappa$ is the von Kármán constant ($\kappa$=0.4), h is the flow depth, z is height above the bed, and $z_0$ is the reference height at which $\overline{U}$ =0. Equation 2 cannot be used for clay flows with strongly modulated turbulence, because the velocity profile of these flows deviates from a logarithmic curve. Instead, $\overline{\overline{U}}$-values for laminar and high-density transitional flows were calculated using the Coles wake function (Coles, 1956; Wang & Plate, 1996; Wang *et al.* 2001):

$$\overline{\overline{U}} = \frac{1}{h - z_0}\int_{z_0}^{h}\left(\overline{U}_{\max} - \frac{u_*}{\kappa}\ln\left(\frac{h}{z}\right) - \frac{2Wu_*}{\kappa}\cos^2\left(\frac{\pi z}{2h}\right)\right) dz \quad (3)$$

where $\overline{U}_{\max}$ is the maximum value of temporal mean velocity and *W* is the wake strength coefficient. In Eq. 3, the von Kármán constant is assumed independent of clay concentration. In the present study, the depth-averaged velocity was between 0.35 and 0.55 m $s^{-1}$ (Table 1), flow depths were ~0.15 m, shear velocities ranged from 0.02 m $s^{-1}$ to 0.09 m $s^{-1}$, and the wake strength coefficient ranged from -0.9 to +0.5.

Siphon tubes connected to peristaltic pumps were used to collect suspension samples to determine the volumetric sediment concentration (Fig. 4) through standard weighing and drying. The suspended sediment concentration, $C_0$, was measured near the bed ~1 minute after flow deceleration. Mean suspended sediment concentration, $C_e$, was calculated from siphon data at six different heights above the bed near the end of the each run, at *t*=2.3 h. The pre-deceleration concentration of non-cohesive sediment within the flows was constant at ~3%, which is well below the Bagnold limit of 9% (Bagnold, 1954); this limit is widely regarded as the threshold for turbulence modulation in non-cohesive sand- and silt-laden flows (e.g., Mulder and Cochonat, 1996). Volumetric kaolin concentrations were between 0.2% and 19.2% (i.e., between 5 g $L^{-1}$ and 500 g $L^{-1}$), encompassing the flow phases where turbulence modulation and full turbulence suppression are expected (Baas *et al.*, 2009). Due to the unstable nature of the bedforms in clay-rich flows (see *Results*), it was impossible to collect bed samples for grain-size analysis.

The Froude number, *Fr*, and flow Reynolds number, *Re*, were calculated to express the basic flow data in dimensionless form:

$$Fr = \frac{\overline{\overline{U}}}{\sqrt{gh}} \quad (4)$$

$$Re = \frac{\overline{\overline{U}} z_p \rho}{\eta} \quad (5)$$

where $g$ is acceleration due to gravity, $\rho$ is flow density, $\eta$ is dynamic viscosity of the flow, and $z_p$ is the thickness of the flow region between the base of the plug flow and the sediment surface. As reasoned in Baas *et al.* (2009), $z_p$ is used in Eq. 5 instead of flow depth, because the largest length scales of turbulence within the transitional and laminar clay flows are limited by the distance between the bed and the base of the plug-flow region. In turbulent flows and turbulence-enhanced transitional flows, in which plug-flow regions are absent, the length scale in Eq. 5 is equal to the flow depth (i.e. $z_p$=$h$). Following Wan (1982), the dynamic viscosity, $\eta$, and yield strength, $\tau_y$, of the suspensions were approximated from the measured suspended-sediment concentrations as:

$$\eta = 0.001 + 0.206\left(\frac{C_0}{100}\right)^{1.68} \quad (6)$$

$$\tau_y = 1280\left(\frac{C_0}{100}\right)^3 \quad (7)$$

Equations 6 and 7 are valid only for kaolin.

The measured bedform data were processed using the methodology proposed by Baas (1994, 1999), with the development of bedform height and wavelength being quantified using the best-fit equations:

$$\frac{H_t}{H_e} = 1 - (0.01)^{\frac{t}{T_e(H)}} \quad (8)$$

$$\frac{L_t - L_0}{L_e - L_0} = 1 - (0.01)^{\frac{t}{T_e(L)}} \quad (9)$$

where $H_t$ and $L_t$ are bedform height and wavelength at time $t$, $H_e$ and $L_e$ are the equilibrium height and wavelength, $L_0$ is the wavelength of the first bedforms appearing on the flat bed, and $T_e(H)$ and $T_e(L)$ are the equilibrium time for height and wavelength, respectively. Following Baas (1994, 1999), the equilibrium time was defined as the time required to reach 99% of the equilibrium bedform height and wavelength. Bedform heights were found to reach equilibrium values well before bedform wavelengths (cf. Baas, 1994, 1999), but part of this difference was caused by inaccuracies in predicting $T_e(L)$- and $L_e$-values due to the fact that some of the experiments were not continued long enough into the stage of fully developed bedforms. This limitation was not a problem for the $T_e(H)$- and $H_e$-data. Therefore, the analysis presented herein uses comparison of wavelength values for mean wavelength values at $t$>1 h only, and for bedform height this method is used in addition to the equilibrium values for height from Eq. 9.

The mean bedform migration rates were converted to a bed sediment flux in order to compare differences in sediment transport rate due to bedform movement below rapidly decelerated turbulent, transitional and quasi-laminar flows using (Van Den Berg, 1987):

$$q_b = \beta(1-p)H_e\overline{u}_c \quad (10)$$

where $q_b$ is the bed sediment flux per unit width, $p$ is bed porosity ($p$=0.35), and $\overline{u}_c$ is mean bedform migration rate for $t$>1 h. $\beta$ is 0.5 for triangular, sandy bedforms, and 0.6 for natural, sandy bedforms (Van Den Berg, 1987), but these values do not necessarily apply to bedforms in cohesive sediment. Therefore, $\beta$ was measured for three randomly chosen bedforms, at the end of Runs 1 to 7, which showed that $\beta$ increased with increasing initial clay concentration from 0.55 to 0.63 (Fig. 6).

## 4. RESULTS

### 4.1. Flow dynamics

The experiments covered the entire range of flow conditions previously documented by Baas *et al.* (2009) from turbulent via transitional to quasi-laminar flow at various suspended sediment concentrations and depth-averaged flow velocities (Table 1). The vertical profiles of $\overline{U}$ and *RMS(u')* correspond well with the profiles expected from their position in the *Re-Fr* phase diagram of Baas *et al.* (2009) (Fig. 1). Run 1, with the lowest clay concentration, produced a 'classic' turbulent flow (TF) with a logarithmic velocity profile and upward-decreasing turbulence intensity (Fig. 7). Runs 2 to 5 were turbulence-enhanced transitional flows (TETF), with *RMS(u')* values up to 13% higher than in Run 1 (e.g. Run 3 in Fig. 7). These TETFs transported between 1.1% and 5.1% suspended sediment (Table 1).

At $C_0$=6.9% and $C_0$=8.0%, Runs 6 and 7 represent lower transitional plug flows (LTPF) with characteristically high *RMS(u')* near the bed (e.g. Run 6 in Fig. 7) and development of a plug flow region near the flow surface (Fig. 8). Figure 8 illustrates that the near-bed *RMS(u')* values increase from the beginning to end of both LTPF experiments. Moreover, it can be seen that a thin plug flow is present above $z$=100 mm (z/h = 0.67) at $t$=0.17 h and $t$=1 h in Run 7, but that a clear vertical velocity gradient has appeared at the same heights after 2 hours. Additionally, the velocity time series of Run 7 clearly changes with time (Fig. 9). At ~6 mm above the bed, the time series shows distinct saw-tooth shaped velocity fluctuations at $t$=0.17 h (cf. Fig. 2), and to a lesser degree at $t$=1 h, but no such fluctuations are present at $t$=2 h (Fig. 9). These observations suggest that both LTPFs become more turbulent in time, and hence move towards higher Reynolds numbers in the clay flow phase diagram.

Run 8, which transported 10.1% sediment, is the only experiment that produced an upper transitional plug flow (UTPF), in which a pronounced plug flow region, moving on top of a layer with reduced turbulence, is apparent from the *RMS(u')* profiles (Fig. 7). At suspended sediment concentrations of ≥12.1%, the turbulence intensities are generally low and the plug flow region is well-developed (e.g. Run 12 in Fig. 7), showing the characteristics of quasi-laminar plug flows (QLPF).

### 4.2 Suspension settling phase

In all experiments, sediment settled rapidly onto the gravel surface directly after the flows were forced to decelerate. Although the resulting deposits were massive, structureless, and had a flat, horizontal surface, their texture changed as the initial suspended sediment concentration was increased. Both the TF and TETFs produced bipartite deposits, consisting of a sandy layer with a thickness of ~9 mm that was overlain by a silty layer of thickness ~5 mm (Fig. 10). Sandy layers of similar thickness were formed also from the decelerated LTPFs and UTPF, but the upper part of these deposits was different. In Run 6 (LTPF), a 7 mm thick muddy, rather than silty, layer developed that consisted of a mixture of silt-sized glass beads and kaolin clay. This layer had the appearance of a fluid mud, with a high water content and high mobility. As the suspended sediment concentration was increased, the thickness of the fluid mud layer increased to 23 mm in the UTPF (Run 8), and its thickness remained between 26 and 34 mm up to $C_0$=19.2% (Run 14, QLPF). The thickness of the sand layer decreased with increasing sediment concentration for the QLPFs, until at $C_0$=16.5% a basal sand no longer formed (Fig. 10); the sand grains were still present but floating in the fluid mud. At relatively low concentrations ($C_0$~11%) in the QLPFs, sand grains visibly moved downward through the fluid mud at a significantly lower rate than in clear water. The fluid mud appeared particularly sandy in Runs 9 to 12 (12.1%<$C_0$<16.5%). Plots of the development of bed thickness for selected high-concentration flows ((UTPF and QLPF; Fig. 11) show that the rate of deposition after flow deceleration (t=0) increased as suspended sediment concentration was increased. Each curve shows rapid development of the bed thickness at $t$<1 h, with the rate of thickness increase becoming higher at greater sediment concentrations, but with the rate of development slowing at $t$>1 h.

### 4.3 Bedform development phase

Bedform development commenced by reworking of the earlier formed bipartite flat bed in the TF, TETFs and LTPFs (Runs 1-7, $C_0 \leq 8$%), but in the UTPF and QLPFs no bedforms were generated, and the fluid-mud dominated beds remained until the end of each experiment (cf. Fig. 11). All the bedforms observed were classified as current ripples, since their height and wavelength were smaller than 60 mm and 600 mm, respectively (Ashley 1990). Figure 12 shows images of the

longitudinal ripple profiles through the flume sidewall in flows with different suspended sediment concentration ($C_0$=0.2%-8.0%, Runs 1, 4, 6 and 7).

The current ripples formed in turbulent flow (Run 1) were asymmetrical in vertical cross-section parallel to the main flow (Fig. 12), with well-developed flow separation being evident at the crest and reverse flow occurring in the ripple trough. As predicted from earlier work (e.g. Baas 1994, 1999), the ripples started to grow at a high rate that then decreased until the equilibrium ripple dimensions were established, thus yielding the typical asymptotic development curves for ripple height and wavelength (Fig. 13). Equilibrium height and wavelength of the bedforms in Run 1 were 13 mm (or 12.9 mm, if based on Eq. 8) and 110 mm, respectively, and the equilibrium height was reached at $t$=0.55 h. The mean migration rate of current ripples in the TF was 0.24 mm $s^{-1}$.

The internal structure of the developing ripples in TF of Run 1 was clearly influenced by the bipartite nature of the initial deposit ($t_0$, Fig. 14). The first small ripples that appeared on the bed were composed entirely of silt-sized sediment ($t_1$, Fig. 14), and bedform growth was controlled mainly by scour in the region of flow reattachment. When the depth of this scour reached the top of the sand layer, the sand grains were then entrained and transported to the downstream ripple crest. This sand accumulated in the crestal region for a short period of time ($t_2$, Fig. 14) before avalanching down the slip face. Silt-sized sediment was also transported along the ripple stoss side and then deposited in the ripple leeside. This process of sand layer scour after initial formation of the ripple produced silty and sandy foreset laminae that were clearly separated at this stage of ripple development, producing a rhythmic alternation in grain size within the cross-sets ($t_3$, Fig. 14) without any fluctuations in the flow velocity. However, at a later stage, when the bedform had migrated over a distance of approximately one ripple wavelength, the sediment became progressively more mixed and the foresets adopted a more uniform composition, becoming less distinct in their grain size differentiation ($t_4$, Fig. 14).

The current ripples in the TETFs possessed an asymmetric form and asymptotic development curves similar to the ripples in the TF, but close inspection of the bedform data also revealed clear differences. As suspended sediment concentration was increased in the TETFs, the equilibrium height and wavelength of the ripples increased, which was closely matched by increases in *RMS(u')* (Figs 15a-b and 15d). The first ripples appeared within several minutes of initial flow deceleration, except for Run 5, in which a delay of 5 minutes was observed. Equilibrium ripple development times for the TETFs varied from 0.5 to 1.5 h. The bed sediment flux in the TETFs decreased with increasing sediment concentration (Fig. 15c), again except for Run 5 ($C_0$=5.1%; Fig. 15c). In Run 5, a trend of increasing bed sediment flux commenced, which continued into the LTPF regime (Fig. 15c). Although recirculation in the leeside separation zone in the TETFs appeared visibly stronger than in the TF, this did not result in any change in internal sedimentary structure, and the temporal development of ripples shown in Fig. 14 also applies to the TETFs. Simons *et al.* (1963) also found that ripple and dune wavelength increased as more bentonite was added to the flow, but that the ripple crests became more rounded as clay concentration increased.

The increase in ripple size at higher suspended sediment concentrations continued into the LTPF regime, culminating in a 41% increase in equilibrium ripple height and an 85% increase in equilibrium ripple wavelength compared to the turbulent flow (at $C_0$=8.0%, Fig. 15a-b). The largest ripple sizes in Run 7 coincide with maximum near-bed *RMS(u')* values in the same run (Fig. 15d). Although both LTPFs showed asymptotic ripple development curves (Fig. 13), there was a considerable delay in the first appearance of bedforms on the initially flat bed. This delay was 0.25 h in Run 6 ($C_0$=6.9%), yet equilibrium height and wavelength were reached well before the end of the experiment. In contrast, equilibrium dimensions may not have been established by the end of Run 7 ($C_0$=8.0%), due to the delayed initiation of bedforms until t=1.7 h (Fig. 13). The ripple height and wavelength for this experiment, shown in Fig. 15a-b, should therefore be regarded as minimum values. The bed sediment flux in Run 6 ($C_0$=6.9%) exhibits a local maximum (Fig. 15c), before dropping dramatically as suspended sediment concentration was increased towards the upper limit of bedform formation (Fig. 15c).

The temporal development of sedimentary structures depicted in Fig. 14 was most pronounced in the LTPFs, but bedform development in these flows was also visibly affected by the presence of fluid mud and strong vorticity in the ripple troughs. In these ripples, reverse flow within the leeside separation zone was strong enough to form prominent backflow ripples on the lower 20% of the slip face (Fig. 16a), which were ~5 mm high and composed of muddy sediment. Avalanching of sandier sediment onto the upper 80% of the slip face led to burial of the backflow ripples, ultimately resulting in preservation of a relatively fine-grained layer with a serrated top surface that lay beneath the silty/muddy sand of the main bedform (Fig. 16a). The cohesive nature of the fluid mud in the bipartite beds of Run 7 ($C_0$=8.0%) was particularly clear from the steeply-dipping stoss sides of the ripples close to the leeside scour of the upstream bedforms (Fig. 16b,c). Moreover, muddy sand and sandy mud was found to drape the irregularly eroded layer of fluid mud in such a way that an asymmetric ripple profile was established (Fig. 16c). Usually, the muddy sand was stored in the upper part of the foresets, while the lower parts consisted of sandy mud (Fig. 16c). These textural and structural properties were typical of the ripples formed at *t*=2.5 h in Run 7, which evolved from ripples with an elongate, convex upward layer of muddy sand on top of the firm mud layer (Fig. 16b; *t*=1.08 h). This muddy sand contained low-angle cross-laminae, while the underlying mud was structureless, except for sub-vertical fluid escape structures (Fig. 16b).

## 5. INTERPRETATION

### 5.1 General

The experimental results presented herein demonstrate that bed development below rapidly waned sediment-laden flows is highly dependent on the cohesive and turbulence forces within the

flow and the textural and rheological properties of the bed. Baas & Best (2008) and Baas *et al.* (2009) have proposed that the balance between cohesive and turbulence forces controls the dynamic properties of clay-rich flows, with cohesive forces increasing at greater suspended clay concentrations due to the electrostatic bonding of electrically-charged clay minerals. At low clay concentrations, turbulence forces generated by shear at the bed-flow interface, and by shear within the flow, are capable of breaking these bonds, but as clay concentration is increased, the bonds eventually become sufficiently strong and spatially-extensive to attenuate turbulence. Turbulence attenuation starts near the top of the flow, where turbulence intensity is lowest, and progressively moves downward with increasing clay concentration, thus forming the plug flows found in flows with >5% suspended sediment (Fig. 7).

The addition of cohesive clay to a non-cohesive sand or silt bed has been found to increase the critical shear stress for sediment entrainment by a factor of up to five (Mitchener & Torfs, 1996). A dramatic increase in sediment shear strength, and thus decrease in erodibility, is also inferred to have been important for the changing flow dynamics in the present experiments. Such changes not only occur from one experimental run to the next (Fig. 15), but also within individual runs, as exemplified by the temporal change of *RMS(u')* profiles within LTPFs (Fig. 8). Furthermore, it is essential to consider changes in the feedback mechanisms between the flow and sediment bed, as a result of changing surface drag and form roughness when ripples develop upon the bed.

### 5.2 Suspension settling phase

After instantaneous flow deceleration from ~50 L $s^{-1}$ to 19 L $s^{-1}$, each flow formed a massive, structureless bed through settling of suspended sediment, thereby generating a flat horizontal surface, but the textural properties of these deposits changed as the initial volume of suspended clay particles increased, particularly in the LTPFs, UTPF and QLPFs. Differences in the settling velocity of the sand and silt particles account for the formation of the bipartite beds in flows carrying up to 5% suspended sediment (Fig. 10). The vast majority of kaolin remained in suspension in the TETFs, although some clay may potentially have settled with the sand and silt or infiltrated into the pore space between the silt and sand grains after deposition. The increased turbulence intensity in the TETFs had no apparent effect on the thickness of the initial sediment bed, suggesting that these flows possessed insufficient turbulence to maintain the sand and silt in suspension. The absence of stratification in the bipartite deposits also attests to rapid sedimentation from waned flows (Middleton, 1967; Arnott & Hand, 1989).

The bipartite beds below the LTPFs also possessed a basal sand layer, but the upper part of these beds consisted of fluid mud rather than silt. This mud consisted of a mixture of kaolin clay and silt-sized particles, and the fluid mud layer began to form immediately after flow deceleration. The fact that these LTPFs are unable to keep all clay particles in suspension can be explained by vertical gradients in the balance between cohesive and turbulence forces. In the upper region of

the flows, cohesive forces are strong enough to attenuate turbulence, particularly at $C_0$=8.0% in Run 7 (Fig. 8), thus leading to a reduction in the turbulence support of silt and clay particles. Such a reduction in particle support is not compensated by an increase in cohesive matrix strength, because the yield strength is too low (Table 1), and therefore the silt and some clay settle out of the flow. This settling process occurs despite the particles having to fall through the lower region of the flow, where turbulence forces are strong and outbalance cohesive forces. However, after entering the lower region, it is difficult for the particles to be transported back upwards, because the LTPFs are strongly stratified and upward mixing is limited to the dissipation of more and more isolated vortices as clay concentration increases (Baas & Best, 2002). In time, progressively more mud accumulates in the lower region of the flow until the concentration is sufficiently high to form a fluid mud on top of the basal sand. The settling of clay into the lower flow region, and therefore the growth of the fluid mud layer, thus appears to be self-limiting, because turbulence gradually re-establishes itself upon removal of clay from the upper flow region, as shown by the increase in *RMS(u')* in the upper half of LTPF of Run 7 from t=0.17 h to t=2 h (Fig. 8).

Early deposition from the UTPF (Run 8, $C_0$=10.1%) occurs in a similar manner to the LTPFs, with sand grains segregating from the finer particles, but within the fine fraction the silt and clay are mixed and form a highly mobile layer of fluid mud. However, the fluid mud layer is considerably thicker than in the LTPFs (Fig. 10), which may be attributed to: (1) the greater availability of kaolin clay, since the initial sediment concentration is higher and the turbulence-attenuated plug flow layer is thicker (Fig. 7) than in the LTPFs; and (2) the drastically reduced near-bed turbulence intensity (Fig. 15d). In the UTPF it thus appears that turbulence forces weaken, and cohesive forces begin to dominate across the entire flow depth, but the cohesive matrix strength is still not high enough to support sand-sized particles. This balance between cohesive and turbulence forces further changes in the QLPFs, where, as concentration increases from $C_0$=12.1%, an increasing amount of sand is incorporated in the fluid mud until a basal sand layer no longer forms at $C_0$=16.5%. The visual observation that sand grains fall at a slow rate through the fluid mud in low-concentration QLPFs, but are supported within the fluid mud in high-concentration QLPFs, suggests that the cohesive matrix becomes progressively stronger and eventually able to support the whole range of particle sizes.

In the present experiments, the medium sand segregated from the kaolin clay at $C_0$<~11%, whilst the sand grains were fully mixed with the fluid mud at $C_0$>~16%. These threshold concentrations for the support of sand-sized particles are similar to the values of 11.3% and 14.3% reported by Sumner *et al.* (2009), who investigated the deposition of sand and clay from continuously decelerating suspension flows at various deceleration times and suspended sand concentrations. The present experimental data show that the threshold concentrations for partial particle segregation and full mixing depend on the grain size of the non-cohesive sediment, since the silt fraction mixed with kaolin clay to form a fluid mud at a lower suspended sediment concentration than the sand fraction (~6% versus ~11%). The phase boundaries between bed

types I (full segregation and structured sand), II (full segregation and structureless sand), III (partial segregation) and IV (no segregation) of Sumner *et al.* (2009; their Fig. 1), which they used to distinguish between turbidites, hybrid beds and debrites, will therefore vary with the available sediment size fractions, as well as the concentration and type of clay, in the original suspension flow.

### 5.3 Bedform development phase

At the mean flow velocity of ~0.46 $ms^{-1}$ used in the present experiments, current ripples formed only in TFs, TETFs and LTPFs (i.e. at suspended sediment concentrations up to 8.0% by volume). Ripples started to develop within several minutes after the beginning of flow deceleration at $C_0$<4%, but at higher concentrations the first appearance of bedforms was delayed, with the time over which the initial flat bed remained stable increasing exponentially from 0.08 h at $C_0$=5.1% to 1.7 h at $C_0$=8.0%. The fluid-mud dominated beds below UTPFs and QLPFs remained stable for the full duration of the experiments. The present results show that the transition from ripples to a cohesive flat bed occurs over a remarkably narrow range of clay concentrations, since large ripples develop at $C_0$=6.9%, but not at $C_0$=8.0%. This cessation of bedform generation can be explained by an increase in bed shear strength, due to the greater amounts of cohesive clay incorporated into the bed, combined with a rapid decline in turbulence intensity across the phase boundary from LTPF to UTPF (Fig. 15d).

After the initial generation of bedforms, the current ripples rapidly increased in height and wavelength, reaching their equilibrium dimensions after approximately one hour at most sediment concentrations. Only near the upper clay concentration limit for bedform formation is it unclear if sufficient time was available to form equilibrium ripples. It is evident that equilibrium ripple height and wavelength increase at greater suspended sediment concentrations within TETFs and LTPFs. This trend is closely matched by near-bed *RMS(u')*, with high $R^2$-values of 0.95 and 0.96 for relationships between near-bed *RMS(u')* and ripple height and wavelength, respectively (Fig. 15). In view of previous work (Baas & Best, 2002, 2008; Baas *et al.* 2009), it is reasoned that the increased near-bed turbulence is caused by a change in flow dynamics inherent to transient turbulent flows, which is dominated by an internal shear layer (cf. Figs 2 and 3). However, another possibility is that the higher near-bed *RMS(u')* values result from higher production of turbulence over the bedforms, because larger ripples produce greater drag. The expected increase in drag coefficient from TF via TETF to LTPF can be estimated using Eqs 11 and 12 (Van Rijn, 1990, 1993):

$$C_d = 18\log_{10}\left(\frac{12h}{k_s''}\right) \tag{11}$$

$$k_s'' = 20\gamma\frac{H_e^{\,2}}{L_e} \tag{12}$$

where $C_d$ is the Chézy drag coefficient , $h$ is flow depth, $k_s''$ is the Nikuradze form roughness height, $\gamma$ is the ripple presence factor ($\gamma$=1 in the present experiments), and $H_e$ and $L_e$ are equilibrium ripple height and wavelength, respectively. Figure 17 illustrates that Eqs 11 and 12 produce a decrease in $C_d$ (indicating increased drag) with increasing suspended sediment concentration, but only of ~2%, thus only making a minor contribution to the production of turbulence. It can therefore be concluded that the bulk of the increase in *RMS(u')* values within TF, TETF and LTPFs is caused by processes related to the presence of an internal shear layer, and that this increase in *RMS(u')* causes the ripples to increase in their height and wavelength. Visually, this contention is supported by the stronger separation zone vortex present in the troughs of ripples formed within TETFs and LTPFs, which appears to enhance bed erosion and produces unusually large backflow ripples (Fig. 16a). Although the increased turbulence intensity within the ripple troughs could not be verified quantitatively in the present experiments, indirect support is provided by the velocity time-series of transitional clay flows collected in the trough of a fixed ripple profile by Baas & Best (2008). These fixed-ripple experiments showed that *RMS(u')* can increase by a factor of two at the point of flow reattachment and by a factor of ten near the base of the separation zone.

It is also worthwhile comparing the trends in near-bed *RMS(u')* from the present experiments with those of the flat bed experiments at similar depth-averaged flow velocities reported by Baas *et al.* (2009; their experimental series 3), since the phase boundary between LTPF and UTPF is at a similar concentration (8.0%<$C_0$<10.1% for the rippled beds herein and 8.9%<$C$<9.6% for the flat beds of Baas *et al.*, 2009). In the flat-bed experiments of Baas *et al.* (2009), near-bed *RMS(u')* increased from 38 mm $s^{-1}$ to 61 mm $s^{-1}$ from the TF to the LTPF-UTPF boundary, while the equivalent increase for the rippled beds detailed herein is from 66 mm $s^{-1}$ to 91 mm $s^{-1}$. This yields an increase in *RMS(u')* of 23 mm $s^{-1}$ and 25 mm $s^{-1}$ for the flat and rippled bed, respectively, with the insignificant difference of 2 mm $s^{-1}$ between the two providing further support for the minor contribution of increasing bed roughness to the enhancement of turbulence.

The bed sediment flux decreases as suspended sediment concentration increases at 0%<$C_0$<3.5% and 7%<$C_0$<10%, but the flux increases between $C_0$~3.5% and $C_0$~7% (i.e. in the high-concentration TETF and LTPF; Fig. 15c). The decreasing bed sediment fluxes are likely controlled by an increase in bed shear strength, and thus a decrease in sediment availability, as progressively larger amounts of cohesive clay are incorporated into the bed. The range of clay concentrations at which the bed sediment flux increases coincides with very high near-bed turbulence intensities, and it is speculated that this produces higher bed shear stresses that increase bed erosion, thus overcoming the high shear strength of the bed. However, since the bed shear strength increases exponentially with clay concentration, this results in another reversal in bed sediment flux at $C_0$>7%. At these high clay concentrations, despite the fact that the LTPF has the highest near-bed turbulence intensity of all the experimental flows, it appears that the bed was stable enough to cause a dramatic decrease in the bed sediment flux (Fig. 15c). Figure 18

summarises the competing forces of turbulence and cohesion in a conceptual model of bed shear strength and near-bed turbulent shear stress. This model assumes that ripples form only if the near-bed turbulent shear stress exceeds the yield strength of the sediment bed, which is expressed in Fig. 18 by the diagonal line of critical shear stress. Ripples can thus form only on the upper left-hand side of this line, with the bed sediment flux due to ripple migration increasing with increasing distance from this shear stress limit. At low yield strengths (e.g. Run 1), near-bed turbulent stresses dominate the bed sediment flux, but near-bed turbulence also works effectively against yield strength in high-concentration TETFs and LTPFs (e.g. Run 6), in spite of the higher bed shear strength. The dip in the bed sediment flux curve for low-concentration TETFs in Fig. 18 represents conditions in which the increasing near-bed turbulent stress cannot keep pace with the increasing yield strength of the bed. The dramatic decrease in near-bed turbulence intensity in UTPFs and QLPFs (Runs 8-14), and the concurrent increase in yield strength, cause the bed sediment flux curve to rapidly cross the critical shear stress limit into the stable flat bed region of Fig. 18.

The laboratory experiments described herein simulated rapidly waning-to-steady mixed-sediment flows, which showed reworking of the deposits formed in the early suspension settling phase through erosion and the generation of current ripple in the bedform development phase. This experimental procedure was different from the procedure used by Sumner *et al.* (2008, 2009), who formed deposits of sand and kaolin clay from suspension flows that decelerated linearly from very high velocity (~3 m $s^{-1}$) to zero velocity. At the typical deceleration time of ~1 minute applied herein, the experiments of Sumner *et al.* (2009) revealed: (i) clean, structureless sand overlain by a mud cap for TF and TETF (their deposit type II); (ii) thin structureless sand overlain by ungraded muddy sand and a mud cap for LTPF and UTPF (their deposit type III); and (iii) ungraded muddy sand with a mud cap for QLPF (their deposit type IV). In addition, Sumner *et al.* (2008, 2009) found that, for type II deposits formed from rapidly decelerated flows, sand segregated from the muddy suspension continuously during flow deceleration and this process continued after the flow had come to a halt. In the rapidly waning-to steady TF and TETF, bedform development commenced almost immediately after the sand and silt had settled from suspension. As these bedforms did not appear to climb upward, it is assumed that most, if not all, of the sand and silt had settled from suspension by the time the first current ripples formed on the bed. The deposits of the rapidly waning-to-steady TF and TETF had a bipartite granulometric texture, with sand overlain by silt (Fig. 10), whereas the equivalent type II deposits of Sumner *et al.* (2008) displayed a normal grading without a clear grain-size break. This textural difference might be caused by the bimodal grain-size distribution of the non-cohesive sediment used in the present experiments (Fig. 5). It thus appears that the type II deposits of Sumner *et al.* (2009) will exhibit cross-stratification if a period of steady flow is present in the flow hydrograph. If such a period of steady flow is able to keep most of the cohesive sediment in suspension, the formation of a protective mud layer on top of the non-cohesive sediment layer will be inhibited, as was found in the type II deposits of Sumner *et al.*

(2009). This lack of protection subsequently permits reworking of the top of the deposit into current ripples. However, it should be straightforward to distinguish the type II deposits with reworked tops from the type I deposits (plane-parallel laminated and cross-laminated sand; Sumner *et al.*, 2008), since reworking will usually be restricted to the maximum depth of scour associated with the bedform troughs. The type III deposits of Sumner *et al.* (2009) contained a thick layer of ungraded muddy sand. Such a layer was absent from the deposits of rapidly waning-to-steady LTPF and UTPF, in which the fluid mud was deprived of sand. The high mobility of the fluid mud, combined with the consistently high levels of turbulence, for especially the LTPF, are inferred to have promoted the deposition through the fluid mud of any sand that remained in suspension after formation of the basal sand layer. Yet, this remaining suspended sand must have constituted small volumes, because the thickness of the basal sand layer in the LTPF and UTPF was similar to that of TF and TETF. Similar to the type II deposits, the type III deposits will exhibit cross-stratification if a period of steady flow is present. Sumner *et al.* (2009) interpreted their type IV deposits as the product of laminar flows that were strong enough to support all non-cohesive sediment. However, it appeared that at least some sand was able to settle onto the bed from the low-concentration rapidly waning-to-steady QLTFs. Again, this might be caused by rheological differences between the rapidly halted flows of Sumner *et al.* (2009) and the present experiments, where an initial rapid waning is followed by a period of steady flow.

## 6. IMPLICATIONS FOR BEDFORMS, FACIES AND HYDRID BED FORMATION

### 6.1. General

The central finding of this experimental study is that bedforms generated in turbulent flows and turbulence-modulated, cohesive flows differ greatly in their size, texture, sedimentary structure and migration rate. The unique properties of the current ripples and plane beds developing below rapidly-waned flows with transient turbulent behaviour documented herein could help to identify such flows and their depositional products, and to interpret key depositional processes, in modern and ancient sediments. Before exploring how these laboratory-based sedimentological data can be used for this purpose, it is important to emphasise that the number of physical variables controlling the dynamics of cohesive mixed sediment is larger than for non-cohesive sediment, and that the experiments herein cover only a subset of these variables. This significantly limits the extrapolation of the results to natural environments, in particular because the experiments comprised: (1) a single clay type, with specific rheological and cohesive properties; (2) a single flow velocity after flow deceleration, that was chosen to specifically position the flows within the current ripple regime; (3) a rapid rate of deceleration, which led to quick, en-masse deposition of the coarse, non-cohesive fraction, in particular at low suspended sediment concentrations; (4) a wide range of grain sizes in the non-cohesive fraction, which accentuated the sedimentary structures produced; (5) a

constant initial volume of non-cohesive suspended sediment; and (6) relatively small total volumes of suspended sediment, resulting in deposits that were thin compared to most natural deposits. The need for additional mixed-sediment research is clear, but despite these limitations, several generic outcomes can be extracted from the experimental data.

### 6.2. Flow Reynolds number and bedform generation

Current ripples develop only in TFs, TETFs and LTPFs, because the turbulent shear stress is high and the bed shear strength is low when compared to UTPFs and QLPFs. In the present experiments, the upper limit of suspended sediment concentration for bedform development was 8%, but this concentration will depend on the flow shear velocity (cf. Baas *et al.*, 2009) as well as the exact composition and size of the sediment. Therefore, neither this concentration, nor any other single value, should be used as a general discriminator of bedform formation, as has been suggested previously for distinguishing turbidity currents from debris flows in deep-marine environments (e.g. Middleton, 1993; Shanmugam, 2000). A better dimensionless approach is to use the flow Reynolds number (Eq. 5), which Baas *et al.* (2009) have shown suitable for delineating the phase boundaries between turbulent, transitional and laminar clay flows. Herein, the Reynolds number at the clay concentration limit for bedform formation is between 8,300 and 19,500, which agrees well with Re=12,000±3,400 for the LTPF-UTPF boundary in the flat-bed experiments of Baas *et al.* (2009). Thus, it can be concluded that the development of current ripples cannot take place in cohesive plug flows with a Reynolds number smaller than 12,000. Bedform development in flows with Re>12,000 will occur only if the bed is formed by the flow itself, as in the present experiments, or if the bed shear stress is higher than the critical shear strength for sediment entrainment of beds that are formed independently. Although the flow Reynolds number approach is particularly useful for predicting mixed sediment facies when the flow properties are known, the reconstruction of flow properties from deposit properties, as needed in sedimentary geology, is more difficult, because it requires independent estimates of the physical parameters that constitute the Reynolds number.

### 6.3. Bedform dimensions and stratification in mixed mud-sand deposits

The equilibrium height and wavelength of the ripples in the TF correspond well with the equilibrium ripple dimensions for 0.095 mm sand quantified by Baas (1994) and those calculated from the current ripple predictors of Baas (1993):

$$H_e = 3.4 \log_{10}(D_{50}) + 18$$

$$L_e = 75.4 \log_{10}(D_{50}) + 197 \quad (13)$$

and Raudkivi (1997):

$$H_e = 18\ D_{50}^{0.1}$$
$$L_e = 245\ D_{50}^{0.35} \quad (14)$$

where $D_{50}$=0.084 mm, and $H_e$ and $L_e$ are equilibrium ripple height and wavelength (in mm), respectively (Table 2). The current ripples in the transitional flows herein were up to 18.3 mm high and 203.0 mm long. Such large dimensions are uncommon for ripples in clean sand, as shown by the predicted height and wavelength of ripples at the upper grain-size limit of ripple formation ($D_{50}$=0.7 mm: Table 2). Ripple height and wavelength might therefore be an appropriate sedimentological discriminator for turbulence-modulated flows, in particular if this is used in combination with other criteria. Transitional-current ripples consist of “dirty”, muddy sand, with the proportion of mud being higher in ripples formed under LTPFs than under TETFs. In the present experiments, the distribution of sand and mud within the ripples was a function of the stage of ripple development (Fig. 14): (1) thin, low-angle, cross-laminated sand that caps the muddy core of ripples is characteristic of early-stage development; (2) rhythmically-interbedded mud-sand cross-laminae represents intermediate-stage development; and (3) mixed mud-sand cross-lamination indicates late-stage development. The type of cross-lamination could therefore be a measure for the duration of bed reworking, and thus flow duration, but this can only be fully assessed when the processes of bedform development at a wider range of waning-to-steady transitional flow conditions have been established. The sequence of stratification types found in the present experiments will exist *only* if a flow forms a deposit with a distinct depositional grain-size break upon rapid deceleration (equivalent to the bipartite beds in the experiments) and if the grain-size break is at a shallower depth than the scour depth of the ripple troughs. Since the maximum scour depth of ripples is of the order of the bedform height, i.e. several tens of millimetres, these sedimentary structures will be confined to thin-bedded deposits (*sensu* McKee and Weir, 1953). Reworking of sediment across a grain-size break might extend to thick- and very-thick bedded bipartite deposits (*sensu* McKee and Weir, 1953) under transitional-flow conditions that allow the development of dunes, since the maximum scour depths of dunes can reach several hundreds of millimetres to several metres. In cases where the mobile bed exists before the clay concentration rises (as opposed to the decelerated flows herein that formed the initial bipartite bed), clays may become incorporated within the deposits. This has been illustrated by Simons *et al.* (1963), who documented clay lenses that were deposited in the ripple troughs, formed from current ripples migrating under bentonite-rich flows.

Other diagnostic criteria for recognising transitional flow deposits in outcrop and core could be more common, and are associated with the characteristically strong near-bed turbulence and cohesive nature of the mixed-sediment beds: (1) Deep erosional scours with steep, irregular edges appear typical of partly cohesive ripples in LTPFs; (2) This irregular topography is often infilled by non-cohesive sand, re-establishing a more triangular ripple shape (Fig. 16c); (3) Anomalously large, fine-grained, backflow ripples (typically 5 mm high) in the troughs of the larger ripples are

preserved as an irregular layer of silt or mud below the foreset cross-laminae (Fig. 16a); and (4) Subvertical, pipe- or sheet-like fluidisation structures within the muddy fraction of the current ripples record the initially rapid deposition of sediment from suspension, followed by dewatering. This fluidisation may be caused by the pressure gradients associated with the strong turbulent velocity fluctuations over the ripple leeside, and possibly aided by loading of sand-silt upon the muddy layer beneath.

### 6.4. Ripple cross-lamination and massive turbiditic sandstones

In a theoretical study of the formation of massive turbiditic sandstones, Baas (2004) suggested that current ripples are ubiquitous below rapidly-decelerating turbidity currents, because these bedforms can form within several tens of seconds. Turbidites should therefore possess a division with ripple cross-lamination, unless there are special circumstances that prevent the formation of the ripples, or that destroy the ripples at a later stage. These speculations may apply not just to turbidites, but also to other deposits that are formed from rapidly-waned flows. The present experiments suggest an alternative mechanism for inhibiting bedform development. If a flow behaves as an UTPF or a QLPF after flow deceleration with Re<12,000, insufficient turbulent shear stresses will exist in order to generate bedforms. Moreover, rapid deceleration of these flows may lead to the deposition of cohesive mud, with the high shear strength of these deposits then further inhibiting bedform development. The bipartite beds shown in Fig. 10 may thus be diagnostic products of UTPFs and QLPFs, although it should be remembered that variations to this sedimentary structure are possible depending on the grain-size distribution in the formative flow, and the degree of segregation of different grain sizes may thus be useful in distinguishing between UTPF and QLPF deposits.

### 6.5. Mixed mud-sand facies of decelerating flows

Although a more comprehensive understanding of the physical variables that control the dynamics of mixed cohesive sediments and their depositional products is required, the laboratory results presented herein can be used to propose preliminary models for the sedimentological properties of natural waning flows that comprise sand, silt and cohesive clay. For this purpose, several schematic sedimentary facies are presented (Fig. 19) that encapsulate variations in the structural and textural features of such deposits as a function of the initial suspended sediment concentration, rate of flow deceleration (based on the above comparison with the work of Sumner *et al.*, 2009), and the duration of post-deceleration steady flow.

Under conditions where the flow decelerates rapidly and the steady flow phase is very short or absent (i.e., equivalent to the continuously and rapidly decelerating flows of Sumner *et al.*, 2009), the sedimentary facies are expected to lack current lamination (Figs 19a-e), but they might show a

basal subfacies with inverse grading, caused by hindered settling (Bagnold, 1956) or kinetic sieving (Middleton, 1970; Legros, 2002) that is overlain by a subfacies with normal distribution grading, caused by differences in grain settling velocity. These textural features are typical of the facies associated with TF and TETF. The sediment size distribution in the formative flow determines if such facies exhibit grain-size breaks (as shown in Fig. 19a) or whether normal grading is more continuous (as in Sumner *et al.*, 2009). In the LTPF and UTPF facies, the finer non-cohesive fraction will be mixed with the cohesive clay fraction to form a mud deposit on top of the basal sand (Figs 19b-c). Evidence for soft sediment deformation within this mud might point to its fluid-mud origin. The basal sand should be relatively thin in the sedimentary facies of mixed-sediment QLPFs (Fig. 19d), or absent altogether (Fig. 19e), as at least part of the sand is incorporated into the cohesive mud. In addition to the presence or absence of the basal sand in the QLPF facies, the clay concentration in the formative flow can also be estimated qualitatively using the vertical distribution of sand in the muddy subfacies, with lower concentration QLPFs producing deposits in which sand tends to accumulate near the base of the mud (Fig. 19d) and higher concentration QLPF deposits exhibiting a more homogeneous distribution of sand grains in the vertical (Fig. 19e).

The inferred sedimentary facies of the rapidly decelerated to steady UTPF and QLPF, shown in Figs 19c-e, are similar to the deposit types III and IV of Sumner *et al.* (2009), which were formed from linearly decelerated flows with a comparable rheology to the present experiments. Sumner *et al.* (2009) demonstrated that these deposit types form at a wide range of flow deceleration rates. It may thus be difficult to estimate the rates of deceleration, or the presence or absence of steady flow phases, from UTPF and QLPF deposits, based solely on their textural properties. In contrast, the rate of flow deceleration and the duration of post-deceleration steady flow could well be reflected in the sedimentary facies of TF, TETF and LTPF. Rapid flow deceleration without a prolonged period of steady flow will produce structureless facies, as described above, but if flow deceleration is more gradual or if a period of steady flow follows the phase of rapid flow deceleration, the TF, TETF and LTPF facies should be stratified (Figs 19f-n). The available laboratory data suggest that the type of stratification depends on the duration of the steady flow phase (Figs 19f-m), and that the stratification will also be different for flows that decelerate continuously at a slow rate (Fig. 19n; Sumner *et al.*, 2009). Steady TFs, TETFs and LTPFs may also be able to rework the original deposit into bedforms that grow in height and length with time by scouring progressively deeper into the underlying structureless facies, thus forming the temporal sequence of sedimentary structures depicted in Figs 14 and 16. The corresponding sedimentary facies (Fig. 19f-m) could thus provide a relative measure for the duration of the steady flow phase. For example, a tripartite bed comprising, from base to top, structureless sand, deformed mud, and low-angle cross stratified sand (Fig. 19i) might signify a steady LTPF of shorter duration than a bipartite bed comprising high-angle cross-stratified sandy mud overlying structureless sand (Fig. 19m). This method for estimating flow duration should however be treated with caution, because

the rate of bedform development is also likely to be dependent on flow velocity (cf. Baas, 1994, 1999), although this dependency has not yet been investigated for mixed sand-mud systems.

### 6.6. Processes controlling the facies of decelerating flows

In sedimentary facies produced by slow, continuous deceleration of TF, TETF and possibly LTPF, Sumner *et al.* (2008, 2009) found that the formation of current lamination takes place simultaneously with sediment deposition. Such facies show evidence of *depositional* sedimentary structures in waning flow, such as Bouma-type sequences (Bouma, 1962), climbing ripples, aggradational upper-stage plane bed laminae, and normal grading (Fig. 19). This is in contrast to the sedimentary facies produced by the rapidly decelerated to steady TF, TETF and LTPF, investigated herein, which should exhibit *erosional* sedimentary structures, such as internal erosional scours and retention of the reworked sediment within the bedform foreset laminae. This evidence for erosion and reworking is expected to occur more frequently near the top of the facies, thus preserving at least some of the original structureless sediment underneath.

All deposits of the experimental TFs, TETFs, LTPFs and UTPFs contain remarkably clean basal sand, suggesting that grain-size segregation directly after flow deceleration is essential for the generation of these deposits. The capacity of these flows to carry non-cohesive sediment is governed mainly by the grain settling velocity (approximated by grain size for the sake of convenience), the magnitude of upward-directed turbulence and the cohesive matrix strength. The turbulence support of sand grains is considered to be of minor importance for the experimental flows investigated herein, because sand quickly settled onto the bed even in the LTPFs, where RMS(u') reached peak values. Full cohesive support of sand grains was found only at suspended sediment concentrations well within the QLPF regime. Silt-sized sediment, however, segregated from the clay suspension only in TF and TETF, but mixed with the suspended clay, and formed fluid mud layers, in the LTPF, UTPF and QLPF facies. Hence, silt grains are supported at lower levels of turbulence and at lower cohesive matrix strength than sand grains, owing to their lower settling velocity. These differences in sediment-carrying capacity, and the effect on sedimentary facies, are depicted graphically in Fig. 20, in which the total grain support is assumed to be equal to the sum of the grain support by upward-directed turbulence and flow cohesion. This approach should be regarded as a first-order approximation, because it ignores the feedback relationships between turbulence and cohesive forces discussed in the introduction. Following Eqs 6 and 7, cohesive support increases exponentially with increasing clay concentration, whilst turbulence support reaches a maximum in LTPF (thin lines in Fig. 20). The total support thus increases at greater clay concentrations in TF, TETF and LTPF, but this trend is interrupted by a decrease in total support for UTPF (thick line in Fig. 20), due to the dramatic decrease in turbulent grain support (cf. Fig. 15) that is inferred to outbalance the increased cohesive support within UTPF. Figure 20 also shows schematically the carrying capacity thresholds for sand and silt, which were

reconstructed using the evidence for size segregation and mixing in the laboratory-derived sedimentary facies. In summary, for the specific experimental conditions considered herein: (a) TF and TETF do not carry any sand or silt, and these size classes are well separated in the corresponding facies; (b) LTPF and UTPF carry silt, but not sand, resulting in a mixed silt-clay (mud) overlying a basal sand in the matching facies; and (c) QLPF carries both sand and silt, with the corresponding facies being dominated by sandy mud. However, it is likely that these facies will vary for different flows and suspended sediments, and it is even possible that facies type boundaries will be crossed. Speculation on the decrease in total carrying capacity of UTPFs (Fig. 20) is particularly fascinating. In these flows, if the flow velocity or sediment concentration is decreased, but the flow remains within the UTPF regime, then the total grain carrying capacity may decrease further than in the present experiments, provoking a change from the bipartite facies shown in Fig. 20 to a facies in which the sand, silt and clay are fully separated, thus resembling the TF and TETF facies. This would defy the common assumption that grain support increases as suspended sediment concentration increases in high-density clay-laden flows, and complicate process reconstructions in the rock record. On the other hand, it could explain the frequent occurrence of basal sands in natural sedimentary facies that are associated with high-concentration sediment gravity flows, such as debrites, high-density turbidity current deposits, and hybrid deposits (*sensu* Haughton *et al.*, 2009).

### 6.7. A revised model for hybrid bed formation

Based on outcrop and core data from a large number of deep-marine sedimentary successions, Haughton *et al.* (2009) proposed an idealised hybrid sediment gravity flow deposit, comprising, from bottom to top (Fig. 21): (a) an H1 division: clean, graded to ungraded, structureless, dewatered sand with a sharp planar base and a top that may be sharp with sand injections or gradational with banding (*sensu* Lowe & Guy, 2000); (b) an H2 division: alternating bands of mud-poor sand and mud-rich sand; (c) an H3 division: muddy sand with mud clasts, sand patches, sand injections, outsized granules and shear fabrics; (d) an H4 division: thin, plane parallel laminated and ripple cross-laminated sand; (e) an H5 division: pseudonodular and/or massive mud. According to Haughton *et al.* (2009), hybrid sediment gravity flow deposits are “emplaced by a combination of fluidal and plastic flow recording switching between turbulent, transitional and laminar behaviour”, following longitudinal flow transformations as sediment gravity flows travel basinward. In the model of Haughton *et al.* (2009), the H1 division is the depositional product of a forerunner turbidity current, the H2 division is formed by a flow with alternating laminar and turbulent behaviour, the H3 division represents a trailing debris flow, and the H4 and H5 divisions are equivalent to Bouma $T_{bc}$ and $T_e$ divisions, thus originating from a low-density turbidity current in the tail of the hybrid event (Fig. 21). Talling *et al.* (2010) described deposits from the outer Mississippi Fan that also comprise a basal clean sand overlain by a debritic mud, but favoured the

model of Sumner *et al.* (2009) for vertical size segregation in cohesive flows over Haughton *et al.* (2009)'s model of longitudinal flow transformation to explain the origin of these beds. The basal clean sand layer was found to terminate at the same location as the overlying debrite, which led Talling *et al.* (2010) to conclude that these divisions were formed by the same flow, i.e. a debris flow with relatively low cohesive matrix strength from which sand particles were able to settle onto the bed (equivalent to deposit type III of Sumner *et al.*, 2009). This genetic model closely matches the formation of the LTPF, UTPF facies in the present laboratory study. The hybrid flow model of Haughton *et al.* (2009) is well documented, but it does not leave much room for vertical segregation of non-cohesive and cohesive size fractions in a single flow type (cf. Figs 19 and 20). It is hypothesised herein that this vertical segregation may take place in conjunction with longitudinal transformation into different turbulent, transitional and laminar flow components (Fig. 21). The structureless H1 division may not be necessarily linked to a forerunner high-density turbidity current (Haughton *et al.*, 2009). A sediment gravity flow that behaves as a rapidly or more gradually decelerating LTPF, UTPF or low-concentration QLPF, and hence with a pronounced plug region instead of pervasive turbulence, will produce a basal sand with textural properties that is similar to the H1 division. These properties include a flat, sharp base, a general lack of internal stratification and a clean texture. The occasional presence of current lamination near the top of H1 divisions and other basal sands (e.g., Talling *et al.*, 2004, 2010) could denote reworking of the sand during a phase of steady flow. Moreover, the banding in the H2 division of hybrid event beds could signify mixing and reworking of cohesive and non-cohesive sediment at the interface of the basal sand and an overlying mobile, possibly sandy, fluid mud in the same flow that formed the basal sand, thus without the need to invoke separate flow components and complex longitudinal fluctuations. The unique character of the H3 division (e.g., large mud clasts, outsized granules and exotic material), as well as the H4 and H5 divisions, precludes a direct relationship with the H1 and H2 divisions. These divisions are therefore most likely to be the product of longitudinal flow transformation (Haughton *et al.*, 2009). However, if the basal structureless sand and the banded subfacies were formed by LTPF or UTPF there may not be such a dramatic longitudinal transition in flow rheology as in the hybrid event model Haughton *et al.* (2009).

## 7. CONCLUSIONS

Flows that contain suspended sediment are ubiquitous within all sedimentary environments and yet there is currently a limited understanding of the influence of high sediment concentrations on the formation of bedforms and their resultant sedimentary structures. Past work has illustrated the unique properties of open-channel flows with transient turbulent behaviour that are present under a wide range of conditions between turbulent flows and those that adopt quasi-laminar flow properties. Additionally, rapidly-decelerated flows of high sediment concentration are not limited to

open-channel flow, and they are likely to occur in many sedimentary environments, for example as a response to flood waning or flow deceleration as bed slope decreases. The present study has sought to investigate the nature of bedform development and deposition under decelerated sediment-laden flows of different clay concentration. Although idealised in their coverage of key variables, these experiments highlight the significant role played by fine sediment concentration in affecting bedform generation, and show that the recognition of deposits formed by these flows in the sedimentary record may be helped by such experimental studies. Ten conclusions can be drawn:

1. The different flow phases defined in past work over smooth walls and fixed bedforms can also be identified over mobile beds with bedform roughness. As clay concentration increases, these flow phases proceed from turbulent flow (TF) to turbulence-enhanced transitional flow (TETF), lower transitional plug flow (LTPF), upper transitional plug flow (UTPF) and finally quasi-laminar plug flow (QLPF).
2. Rapid initial sedimentation always forms planar beds, with the nature of these beds a function of the nature of the flow phase. These facies are similar to those presented by Sumner *et al.* (2009), although it is shown herein that their phase boundaries will vary as a function of sediment size fractions, as well as clay concentration and clay type. These initial planar beds may be reworked into rippled beds, if a period of steady flow is present. With increasing suspended clay concentration, ripples first increase in height and wavelength under TETF and LTPF regimes, which is attributed to the additional turbulence generated under these flows that cause greater leeside erosion.
3. As clay concentration increases further from LTPF, ripples quickly cease to exist under the UTPF and QLPF conditions investigated herein. This appears due to turbulence suppression as the nature of the flow changes, as well as due to the increasing shear strength of the bed sediment that becomes more difficult to erode as clay concentration increases.
4. With increasing suspended sediment concentration, the flux of bedload sediment first decreases, due to increased bed shear strength, and then increases, due to enhanced near-bed turbulence and subsequent increased erosion rate, but eventually falls rapidly as both turbulence suppression and the shear strength of the bed increase.
5. The stratification within ripples formed under rapidly-decelerated to steady transitional flows reflects the availability of sediment from a bipartite bed that initially consists of settled medium sand and then fine sediment. The exact nature of the ripple cross-stratification in these flows is a direct function of the duration of the formative flow.
6. Current ripples cannot form in cohesive plug flows with a flow Reynolds number smaller than 12,000, and in this case beds lacking any cross-lamination are likely to form on flow deceleration.

7. No single sediment concentration can be used to discriminate different types of bedform formation in transitional flows, because the development of bedforms is also governed by the flow shear velocity and the physical properties of the suspended and bed sediment.
8. A new facies model for decelerated cohesive (sand-mud) sediment flows is outlined that accounts for suspended clay concentration, initial rate of deceleration, and the duration of any post-deceleration steady flow.
9. A conceptual model of sediment segregation and mixing for mixed cohesive sediment flows is proposed. This model suggests that there may not always be a continuous increase in grain support within the flow as clay concentration increases. Such variation in grain support with sediment concentration may be a key mechanism that enables clean sands to be deposited at the base of high-concentration mud-rich gravity flows.
10. A new model for hybrid beds is proposed that explains the previously documented structural and textural features (*sensu* Haughton *et al.*, 2009) in terms of a combination of vertical segregation and longitudinal flow transformation.

The present study has presented the first fully quantitative data on mobile bed sedimentation, and the first experimental data on bedform stratification, formed by decelerated sediment-laden flows, but under a restricted range of flow conditions. Further work is urgently required to expand the range of flow boundary conditions, and hence deposits and bedforms studied, to include dune-scale bedforms, as well as how these bedforms are represented within the ancient sedimentary record. The preliminary facies models, and the conceptual model of segregation and mixing, presented herein should assist in extrapolating the experimental data to natural processes and products.

## 8. ACKNOWLEDGEMENTS

We are very grateful to the UK Natural Environment Research Council for grant NE/C514823/1 that enabled this research to be undertaken at the Sorby Environmental Fluid Dynamics Laboratory, whilst JHB and JLB were at Leeds. Gareth Keevil is thanked for his support in the laboratory. We also acknowledge the thorough and highly stimulating comments on an earlier version of this paper by Esther Sumner, Joris Eggenhuisen, Associate Editor Peter Talling, Journal Editor Stephen Rice, and an anonymous reviewer.

## 9. REFERENCES

**Amy, L.A.** and **Talling, P.J.** (2006) Anatomy of turbidites and linked debrites based on long distance (120X30 km) bed correlation, Marnoso Arenacea Formation, northern Apennines, Italy. *Sedimentology*, **53,** 161-212.

**Amy, L.A., Talling, P.J., Peakall, J., Wynn, R.B.,** and **Arzola Thynne, R.G.** (2005) Bed geometry used to test recognition criteria of turbidites and (sandy) debrites. *Sedimentary Geology*, **179**, 163-174.

**Arnott, R.W.C.** and **Hand, B.M.** (1989) Bedforms, primary structures and grain fabric in the presence of suspended sediment rain. *Journal of Sedimentary Petrology*, **59,** 1062-1069.

**Ashley, G.M.** (1990) Classification of large-scale subaqueous bedforms: a new look at an old problem. *Journal of Sedimentary Petrology*, **60,** 160-172.

**Baas, J.H.** (1993) Dimensional analysis of current ripples in recent and ancient depositional environments. *Geologica Ultraiectina*, **106,** 199 pp.

**Baas, J.H.** (1994) A flume study on the development and equilibrium morphology of small-scale bedforms in very fine sand. *Sedimentology*, **41,** 185-209.

**Baas, J.H.** (1999) An empirical model for the development and equilibrium morphology of current ripples in fine sand. *Sedimentology*, **46,** 123-138.

**Baas, J.H.** (2004) Conditions for formation of massive turbiditic sandstones by primary sedimentary processes. *Sedimentary Geology*, **166**, 293-310.

**Baas, J.H.** and **Best, J.L.** (2002) Turbulence modulation in clay-rich sediment-laden flows and some implications for sediment deposition. *Journal of Sedimentary Research*, **72,** 336-340.

**Baas, J.H.** and **Best, J.L.** (2008) The dynamics of turbulent, transitional and laminar clay-laden flow over a fixed current ripple. *Sedimentology*, **55,** 635-666.

**Baas, J.H.** and **Best, J.L.** (2009) On the flow of natural clay suspensions over smooth and rough beds. *ERCOFTAC Bulletin*, **78**, 58-63.

**Baas, J.H., Best, J.L., Peakall, J.** and **Wang, M.** (2009) A phase diagram for turbulent, transitional, and laminar clay suspension flows. *Journal of Sedimentary Research*, **79,** 162-183.

**Bagnold, R.A.** (1954) Experiments on a gravity-free dispersion of large, solid spheres in a Newtonian fluid model shear. *Royal Society of London, Proceedings*, **A225**, 49-63.

**Bagnold, R.A.** (1956) The flow of cohesionless grains in fluids. *Royal Society of London, Philosophical Transactions*, **A249**, 235-297.

**Best, J.L.** (1992) Sedimentology and event timing of a catastrophic volcaniclastic mass flow, Volcan Hudson, Southern Chile. *Bulletin of Volcanology*, **54,** 299-318.

**Best, J.L., Kirkbride, A.D.** and **Peakall, J.** (2001) Mean flow and turbulence structure of sediment-laden gravity currents: new insights using ultrasonic Doppler velocity profiling. In: *Particulate Gravity Currents* (Eds W.D. McCaffrey, B.C. Kneller and J. Peakall), *IAS Special Publications,* **31**, 159–172.

**Bouma, A.H.** (1962) *Sedimentology of Some Flysch Deposits: a Graphic Approach to Facies Interpretation*. Elsevier, Amsterdam, 168 pp.

**Coles, D.** (1956) The law of the wake in the turbulent boundary layer. *Journal of Fluid Mechanics*, **1**, 191-226.

**Dasgupta, P.** (2003) Sediment gravity flow - the conceptual problems. *Earth-Science Reviews*, **62,** 265-281.

**Haughton, P., Davis, C., McCaffrey, W.** and **Barker, S.** (2009) Hybrid sediment gravity flow deposits - Classification, origin and significance. *Marine and Petroleum Geology*, **26,** 1900-1918.

**Legros, F.** (2002) Can dispersive pressure cause inverse grading in grain flows? *Journal of Sedimentary Research*, **72**, 166-170.

**Liu, K.F.** and **Mei, C.C.** (1990) Approximate equations for the slow spreading of a thin sheet of Bingham plastic fluid, *Physics of Fluids*, **A2**, 30-36.

**Lowe, D.R.** and **Guy, M.** (2000) Slurry-flow deposits in the Britannia Formation (Lower Cretaceous), North Sea: a new perspective on the turbidity current and debris flow problem. *Sedimentology*, **47,** 31-70.

**McKee, E.D.** and **Weir, G.W.** (1953) Terminology for stratification and cross-stratification in sedimentary rocks. *Geological Society of America Bulletin*, **64**, 381-389.

**Middleton, G.V.** (1967) Experiments on density and turbidity currents. III. Deposition of sediment. *Canadian Journal of Earth Sciences*, **4,** 475-505.

**Middleton, G.V.** (1970) Experimental studies related to problems of flysch sedimentation. In: Flysch Sedimentology in North America (Ed. J. Lajoie), *Geological Association of Canada, Special Paper*, **7**, 253-272.

**Middleton, G.V.** (1993) Sediment deposition from turbidity currents. *Annual Review of Earth Sciences*, **21,** 89-114.

**Mitchener, H.** and **Torfs, H.** (1996) Erosion of mud/sand mixtures. *Coastal Engineering*, **29,** 1-25.

**Mulder, T.** and **Alexander, J.** (2001) The physical character of subaqueous sedimentary density flows and their deposits. *Sedimentology*, **48**, 269-299.

**Mulder, T.** and **Cochonat, P.** (1996) Classification of offshore mass movements. *Journal of Sedimentary Research*, **66,** 43-57.

**Packman, A. I. and MacKay, J. S.** (2003) Interplay of stream-subsurface exchange, clay particle deposition, and streambed evolution, *Water Resources Research*, **39**, 1097-1105.

**Pierson, T.C.** and **Scott, K.M.** (1985) Downstream dilution of a lahar: Transition from debris flow to hyperconcentrated streamflow. *Water Resources Research*, **21,** 1511-1524.

**Raudkivi, A.J.** (1997) Ripples on stream bed. *Journal of hydraulic Engineering*, **123,** 58-64.

**Shanmugam, G.** (2000) 50 years of the turbidite paradigm (1950s-1990s): deep-water processes and facies models - a critical perspective. *Marine and Petroleum Geology*, **17,** 285-342.

**Simons, D.B., Richardson, E.V.** and **Haushild, W.L.** (1963) *Some effects of fine sediment on flow phenomenae*. US Geol Survey Water Supply Paper 1498-G, 45pp.

**Stow, D.A.V.** and **Johansson, M.** (2000) Deep-water massive sands: nature, origin and hydrocarbon implications. *Marine and Petroleum Geology*, **17,** 145-174.

**Sumner, E.J., Amy, L.A.** and **Talling, P.J.** (2008) Deposit structure and processes of sand deposition from decelerating sediment suspensions. *Journal of Sedimentary Research*, **78**, 529-547.

**Sumner, E.J., Talling, P.J.** and **Amy, L.A.** (2009) Deposits of flows transitional between turbidity current and debris flow. *Geology*, **37**, 991-994.

**Takeda, Y.** (1991) Development of an ultrasound velocity profile monitor. *Nuclear Engineering and Design*, **126**, 277-284.

**Talling, P.J., Amy, L.A., Wynn, R.B., Peakall, J.** and **Robinson, M.** (2004) Beds comprising debrite sandwiched within co-genetic turbidite: origin and widespread occurrence in distal depositional environments. *Sedimentology*, **51,** 163-194.

**Talling, P.J., Wynn, R.B., Schmmidt, D.N., Rixon, R., Sumner, E.** and **Amy, L.** (2010) How did thin submarine debris flows carry boulder-sized intraclasts for remarkable distances across low gradients to the far reaches of the Mississippi Fan? *Journal of Sedimentary Research*, **80,** 829-851.

**Traykovski, P., Geyer, W.R., Irish, J.D.** and **Lynch, J.F.** (2000) The role of wave-induced density-driven fluid mud flows for cross-shelf transport on the Eel River continental shelf. *Continental Shelf Research*, **20,** 2113-2140.

**Van Den Berg, J.H.** (1987) Bedform migration and bed-load transport in some rivers and tidal environments. *Sedimentology*, **34**, 681-698.

**Van Maren, D.S., Winterwerp, J.C., Wang, Z.Y.** and **Pu, Q.** (2009) Suspended sediment dynamics and morphodynamics in the Yellow River, China. *Sedimentology*, **56**, 785-806.

**Van Rijn, L.C.** (1990) *Principles of Fluid Flow and Surface Waves in Rivers, Estuaries, Seas and Oceans*. Aqua Publications, Amsterdam, 335 pp.

**Van Rijn, L.C.** (1993) *Principles of Sediment Transport in Rivers, Estuaries and Coastal Seas*. Aqua Publications, Amsterdam, 700 pp.

**Wan, Z.** (1982) *Bed material movement in hyperconcentrated flow.* Institute of Hydrodynamics and Hydraulic Engineering, Lyngby, Technical University of Denmark, Series Paper, pp. 16–24.

**Wang, X., Wang, Z.Y., Yu, M.,** and **Li, D.** (2001) Velocity profile of sediment suspensions and comparison of log-law and wake-law. *Journal of Hydraulic Research*, **39**, 211-217.

**Wang, Z.** and **Plate, E.J.** (1996) A preliminary study on the turbulence structure of flows on non-Newtonian fluid. *Journal of Hydraulic Research*, **34,** 345-361.

## FIGURE CAPTIONS

**Table 1** – Experimental parameters.

**Table 2** – Comparison of equilibrium ripple dimensions.

**Figure 1** – Clay flow phase diagram of Baas *et al.* (2009). The coloured symbols denote flows investigated in the present paper.

**Figure 2** – Schematic models of turbulent, transitional and quasi-laminar clay flows over a smooth, flat bed. The graphs to the left of the models denote characteristic velocity time series at various heights in the flows. The graphs to the right of the models represent characteristic vertical profiles of dimensionless downstream velocity ($\overline{U}/\overline{U}_{\max}$) and root-mean-square of downstream velocity (*RMS(u')*). Modified after Baas *et al.* (2009).

**Figure 3** - Conceptual models showing the changing dynamics of flow in the leeside of a fixed, flow-transverse bedform, as a function of increasing clay concentration. Modified after Baas & Best (2008).

**Figure 4** – Schematic diagram of the experimental set-up. UDVP = Ultrasonic Doppler Velocity Profilers.

**Figure 5** – Grain-size distribution curves of the cohesive and non-cohesive fractions used in the experiments. The frequencies for both fractions add up to 100%. The size class width is 1/6$\phi$. The non-cohesive fraction was prepared by mixing two types of spherical glass beads ($D_{50}$=0.044 mm and $D_{50}$=0.084 mm) with two types of natural medium sand ($D_{50}$=0.283 mm and $D_{50}$=0.310 mm) in order to produce a sediment with a wide range of grain sizes.

**Figure 6** – Initial clay concentration plotted against $\beta$ that is used in Eq. 10. The dashed lines indicate one standard deviation around the mean.

**Figure 7** – Vertical profiles of time-averaged downstream flow velocity (top) and the root-mean-square of downstream velocity (bottom) for selected experimental runs.

**Figure 8** - Vertical profiles of the root-mean-square of downstream velocity for lower transitional plug flows. Note that *RMS(u')*-values change with time.

**Figure 9** – Time series of downstream velocity at ~6 mm above the bed in Run 7 ($C_0$=8.0%) at 3 different points in time. Note the pronounced saw-tooth shaped velocity fluctuations at $t$=0.17 h, and to a lesser degree at $t$=1 h.

**Figure 10** – Thickness and textural features of deposits formed after rapid flow deceleration and just before bedform development commenced. The question mark denotes estimated thickness, because of difficulties in recognising the flow-bed interface. Scale on photograph is in inches (top) and centimetres (bottom). The information above the graph refers to the boundary concentration for bedform development that occurred after the formation of the initial flat bed.

**Figure 11** – Temporal development of fluid mud layer thickness in the upper transitional plug flow and the quasi-laminar plug flows.

**Figure 12** – Sidewall photographs of final bedforms in selected experimental runs. Note the increase in ripple height and wavelength with increasing suspended sediment concentration and the muddy character of the ripple cores in Run 7 ($C_0$=8.0%, shown by light colours).

**Figure 13** – Bedform height and wavelength development curves for selected runs in one turbulent flow and three lower transitional plug flows. Dashed lines indicate one standard deviation around the mean.

**Figure 14** – Photographs and schematic drawings of bedforms in progressive stages of development starting from an initial flat bed. The drawings are valid for TF, TETF and LTPF. The photographs are from Run 6 ($C_0$=6.9%), in which the fine-grained top of the initial flat bed (at t=0.26 h) was more cohesive than in runs with lower suspended clay concentrations. Scale on photographs is in inches (top) and centimetres (bottom).

**Figure 15** - Relationships between initial suspended sediment concentration and (a) equilibrium bedform height, (b) equilibrium bedform wavelength, (c) bed sediment flux and (d) *RMS(u')*.

**Figure 16** – (a) Schematic drawing of a current ripple with prominent backflow ripples in Run 6 ($C_0$=6.9%). This ripple corresponds to the bedform at $t_4$ in Fig. 14. Not to scale. (b) Photograph and labelled drawing of characteristic bedforms in Run 7 ($C_0$=8.0%) at $t$=1.08 h. (c) Photograph and labelled drawing of characteristic bedforms in Run 7 at $t$=1.5 h. Note that the core of firm mud in (b) and (c) affects bedform properties. See text for details.

**Figure 17** – Relationship between initial suspended sediment concentration and Chézy coefficient calculated for the experimental bedform heights and wavelengths.

**Figure 18** – Conceptual model explaining variations in bed sediment flux as function of yield strength and near-bed turbulent stress. The length of the arrows to the left and above the critical shear stress line is a measure of the bed sediment flux.

**Figure 19** – Schematic sedimentary logs of mixed sand-mud facies produced by decelerated high-density flows, organised according to initial suspended sediment concentrations, duration of post-deceleration steady flow, and deceleration rate. Text in red boxes summarises principal facies types (flat, stratified, structureless) and formation mechanism. Text in green boxes summarises possible types of deceleration. See main text for details. C = concentration.

**Figure 20** – Conceptual model for segregation and mixing of particle size fractions in mixed cohesive sediment flows and their sedimentary facies, based on the inferred turbulent and cohesive carrying capacity of flows with different suspended clay concentration. Total grain support (thick line) is assumed to be equal to the sum of turbulence support and cohesive support (thin lines). Turbulence support for LTPF is subdivided into the part close to the bed (thin solid black line) and the part in the overlying rigid plug (thin dashed black line); see Fig. 2.

**Figure 21** – Schematic log of idealised hybrid event bed with inferred processes of formation of H1-H5 divisions, based on Haughton *et al.* (2009) and this study. Modified after Haughton *et al.* (2009).

**Table 1** - Experimental parameters

| Run | Duration (h) | T (º C) | $C_0$ (vol%) | $C_0$ (g $L^{-1}$) | $C_e$ (vol%) | $\eta$ [1] (Ns $m^{-2}$ x$10^{-3}$) | $\tau_y$ [1] (N $m^{-2}$) | h (m) | $z_p$ (m) | f(UDVP) (Hz) | U (mm $s^{-1}$) | $U_{max}$ (mm $s^{-1}$) | Fr (-) | Re [1] (-) | Slope x$10^{-3}$ | Flow phase |
|---|---|---|---|---|---|---|---|---|---|---|---|---|---|---|---|---|
| 1 | 2.85 | 19.3 | 0.2 | 5.2 | 0.04 | 1.006 | 0.000 | 0.151 | 0.151 | 115 | 465 | 566 | 0.38 | 69939 | 1.38 | TF |
| 2 | 2.67 | 19.9 | 1.1 | 28.6 | 0.75 | 1.106 | 0.002 | 0.150 | 0.150 | 115 | 453 | 573 | 0.37 | 62434 | 1.38 | TETF |
| 3 | 2.52 | 19.9 | 1.7 | 44.2 | 1.5 | 1.219 | 0.006 | 0.151 | 0.151 | 115 | 445 | 539 | 0.37 | 56610 | 1.38 | TETF |
| 4 | 2.48 | 19.6 | 3.5 | 91.0 | 3.1 | 1.738 | 0.055 | 0.150 | 0.150 | 115 | 448 | 556 | 0.37 | 40918 | 1.38 | TETF |
| 5 | 2.50 | 18.9 | 5.1 | 132.6 | 4.6 | 2.389 | 0.170 | 0.149 | 0.149 | 115-116 | 425 | 534 | 0.35 | 28675 | 1.38 | TETF |
| 6 | 2.50 | 19.1 | 6.9 | 179.4 | 6.8 | 3.307 | 0.420 | 0.147 | 0.147 | 118 | 440 | 509 | 0.37 | 21769 | 1.38 | LTPF |
| 7 | 2.48 | 18.7 | 8.0 | 208.0 | 8.0 | 3.958 | 0.655 | 0.150 | 0.150 | 119-130 | 456 | 569 | 0.38 | 19530 | 1.38 | LTPF |
| 8 | 2.52 | 18.7 | 10.1 | 262.6 | 9.3 | 5.377 | 1.319 | 0.140 | 0.071 | 130-132 | 543 | 579 | 0.46 | 8329 | 1.38 | UTPF |
| 9 | 2.47 | 19.8 | 12.1 | 314.6 | 10.9 | 6.929 | 2.268 | 0.139 | 0.051 | 132 | 545 | 568 | 0.47 | 4788 | 0.29 | QLPF |
| 10 | 2.50 | 19.1 | 13.8 | 358.8 | 12.5 | 8.394 | 3.364 | 0.140 | 0.036 | 132 | 511 | 539 | 0.44 | 2676 | 1.38 | QLPF |
| 11 | 2.53 | 19.9 | 15.4 | 400.4 | 14.0 | 9.890 | 4.675 | 0.140 | 0.036 | 132 | 496 | 504 | 0.42 | 2250 | 1.81 | QLPF |
| 12 | 2.50 | 19.9 | 16.5 | 429.0 | 15.5 | 10.983 | 5.750 | 0.146 | 0.031 | 133 | 443 | 447 | 0.37 | 1581 | 2.85 | QLPF |
| 13 | 2.52 | 20.1 | 18.2 | 473.2 | 17.3 | 12.770 | 7.717 | 0.146 | 0.026 | 133 | 351 | 353 | 0.29 | 923 | 3.26 | QLPF |
| 14 | 2.55 | 20.5 | 19.2 | 499.2 | 18.2 | 13.877 | 9.060 | 0.150 | 0.019 | 133 | 447 | 449 | 0.37 | 800 | 4.24 | QLPF |

T = mean fluid temperature
$C_0$ = initial suspended sediment concentration (t~1 min)
$C_e$ = final depth-averaged suspended sediment concentration (t = 2.3 h)
$\eta$ = dynamic viscosity
$\tau_y$ = yield stress
h = flow depth
$z_p$ = height of base of plug flow region
f(UDVP) = (range of) frequency of velocity data
U = depth-averaged velocity
[1] This parameter is calculated using $C_0$.

$U_{max}$ = maximum velocity in vertical profile
Fr = Froude number
Re = flow Reynolds number after Liu & Mei (1990)
TF = turbulent flow
TETF = turbulence-enhanced transitional flow
LPTPF = lower-phase transitional plug flow;
UPTPF = upper-phase transitional plug flow
QLPF = quasi-laminar plug flow

**Table 2** - Comparison of equilibrium ripple dimensions

| Source | Equilibrium ripple height (mm) | Equilibrium ripple wavelength (mm) |
|---|---|---|
| This study, TF | 13.0 | 109.8 |
| Baas (1993) predictor | 14.3 | 115.9 |
| Baas (1994) for $D_{50}$=0.095 mm | 13.1 | 115.7 |
| Raudkivi (1997) predictor | 14.1 | 103.0 |
| This study, LTPF | 18.3 | 203.2 |
| Baas (1993) predictor, upper limit (0.7 mm sand) | 17.5 | 185.3 |
| Raudkivi (1997) predictor, upper limit (0.7 mm sand) | 17.4 | 216.2 |

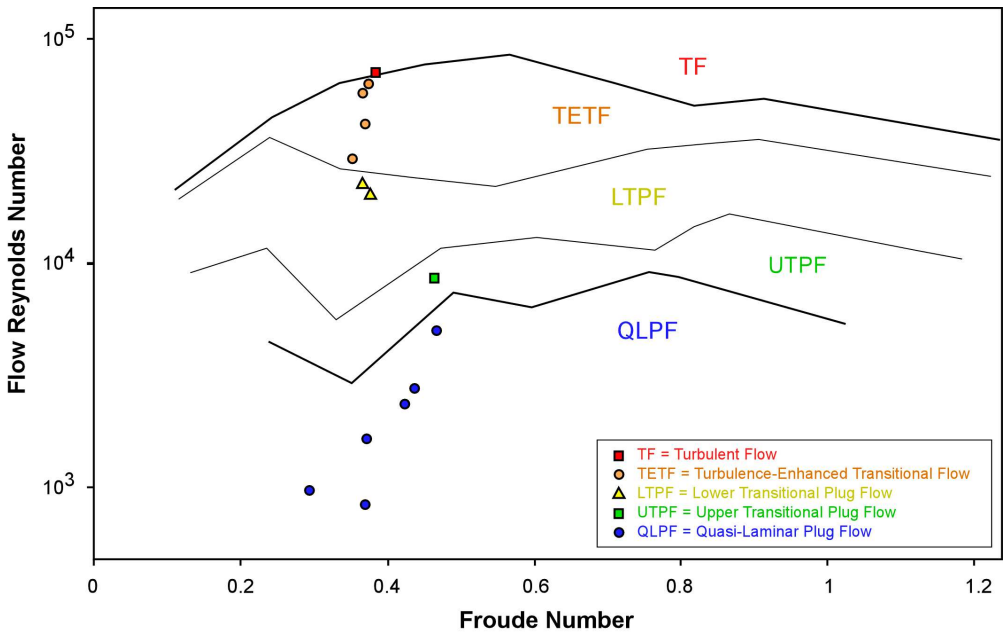


Figure 1 – Clay flow phase diagram of Baas et al. (2009). The coloured symbols denote flows investigated in the present paper.
180x112mm (300 x 300 DPI)

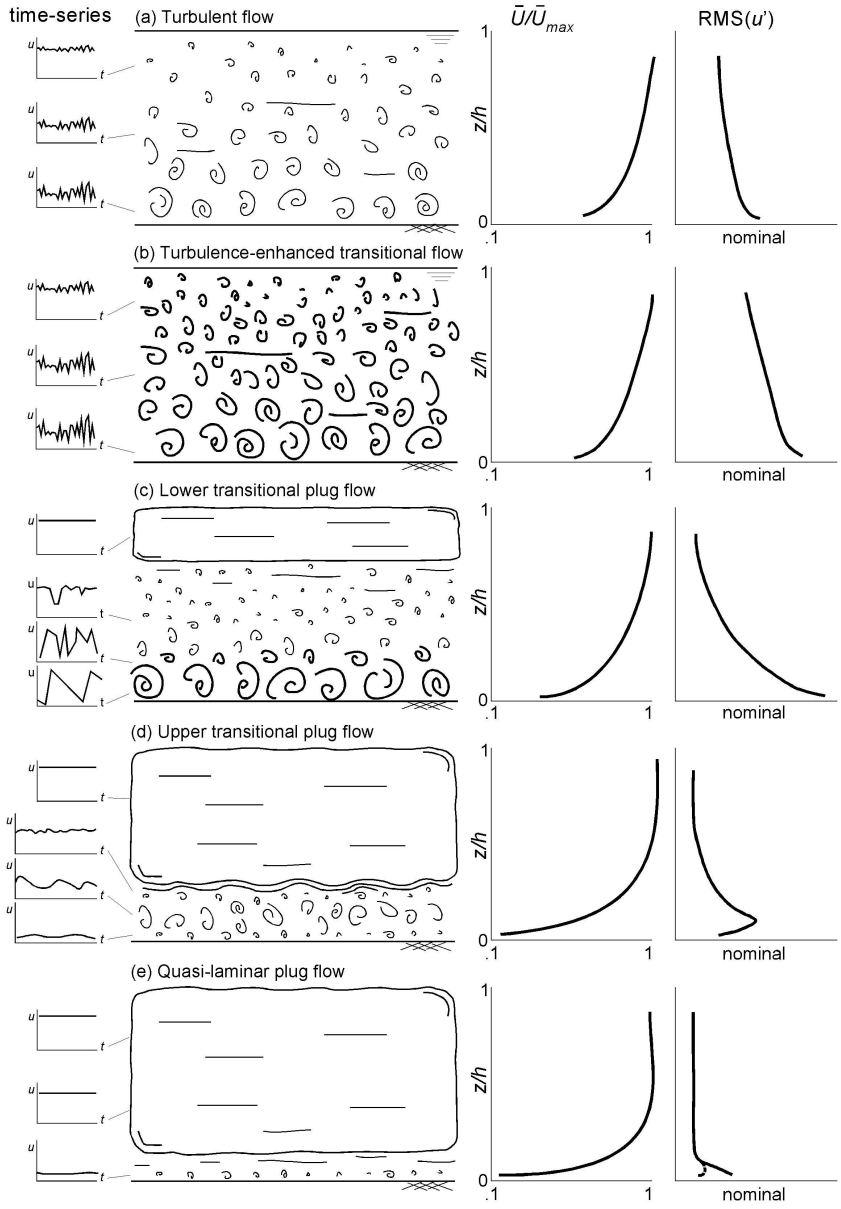


Figure 2 – Schematic models of turbulent, transitional and quasi-laminar clay flows over a smooth, flat bed. The graphs to the left of the models denote characteristic velocity time series at various heights in the flows. The graphs to the right of the models represent characteristic vertical profiles of dimensionless downstream velocity ( U/Umax) and root-mean-square of downstream velocity (RMS(u')). Modified after Baas et al. (2009).
194x280mm (300 x 300 DPI)

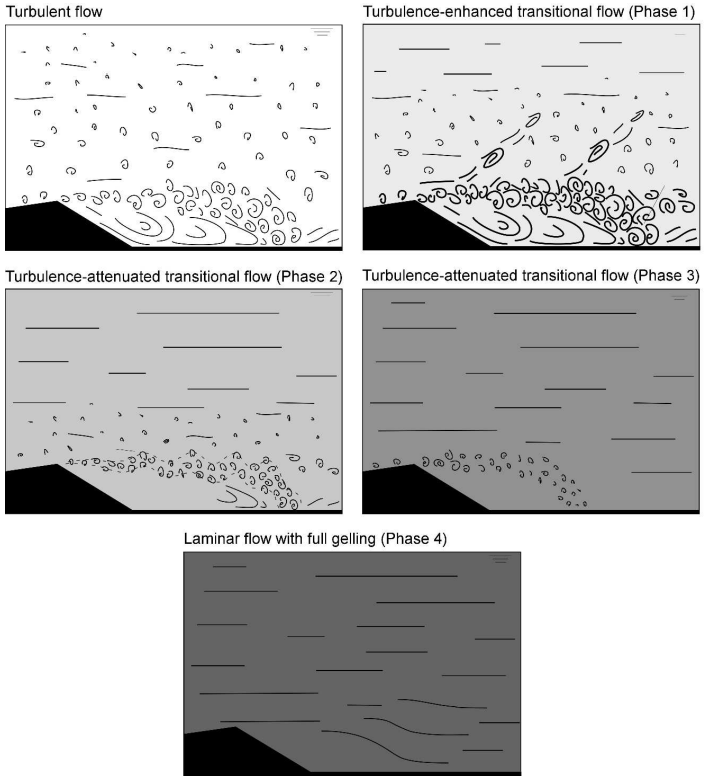


Figure 3 - Conceptual models showing the changing dynamics of flow in the leeside of a fixed, flow-transverse bedform, as a function of increasing clay concentration. Modified after Baas & Best (2008).
320x247mm (300 x 300 DPI)

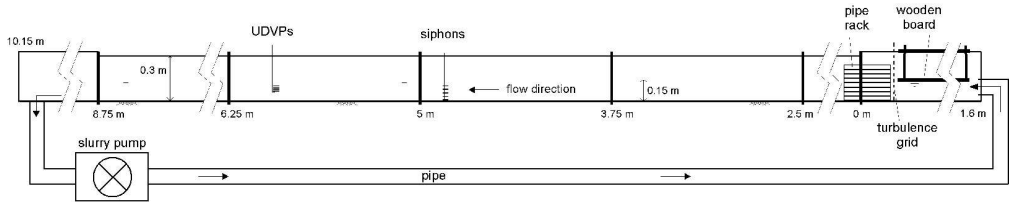


Figure 4 – Schematic diagram of the experimental set-up. UDVP = Ultrasonic Doppler Velocity Profilers.
274x54mm (300 x 300 DPI)

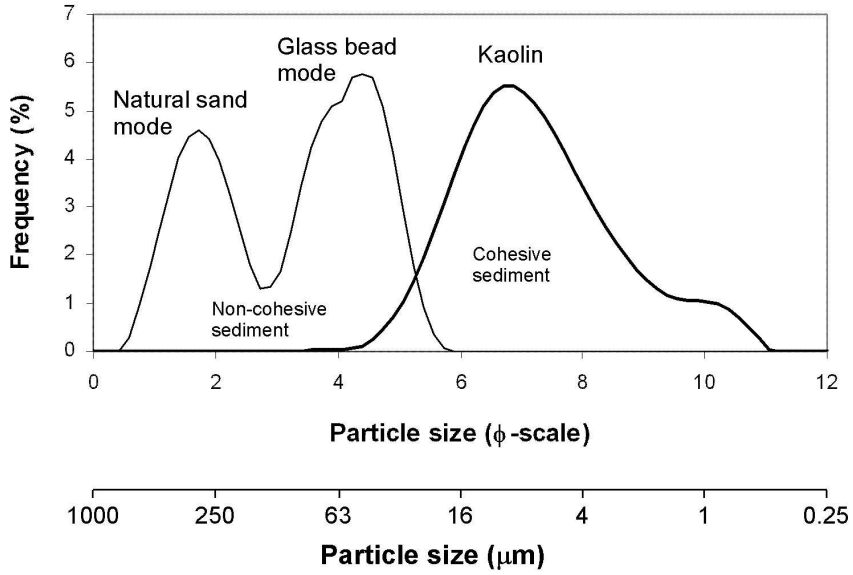


Figure 5 – Grain-size distribution curves of the cohesive and non-cohesive fractions used in the experiments. The frequencies for both fractions add up to 100%. The size class width is 1/6φ. The non-cohesive fraction was prepared by mixing two types of spherical glass beads (D50=0.044 mm and D50=0.084 mm) with two types of natural medium sand (D50=0.283 mm and D50=0.310 mm) in order to produce a sediment with a wide range of grain sizes.
148x89mm (300 x 300 DPI)

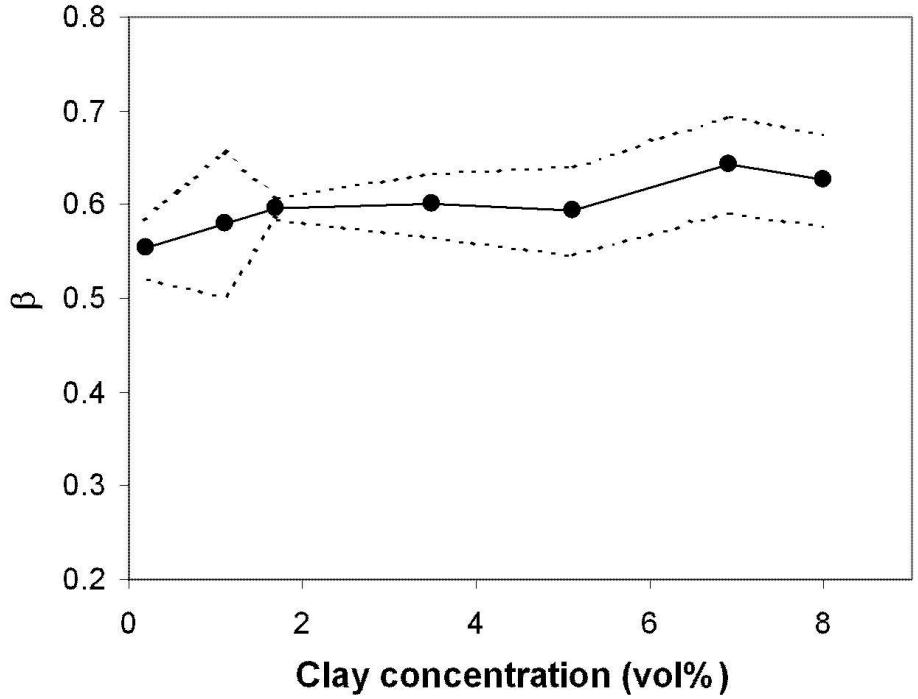


Figure 6 – Initial clay concentration plotted against β that is used in Eq. 10. The dashed lines indicate one standard deviation around the mean.
115x88mm (300 x 300 DPI)

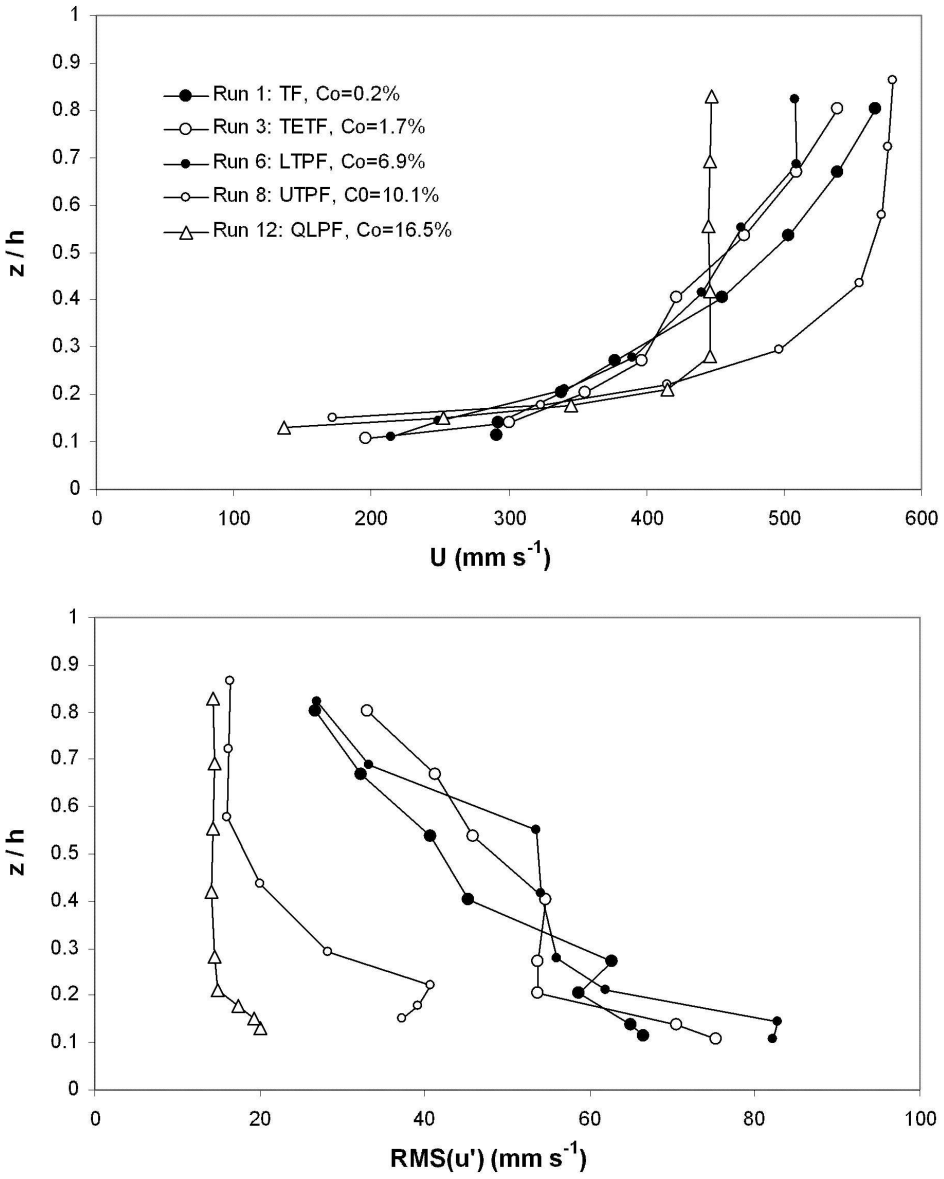


Figure 7 – Vertical profiles of time-averaged downstream flow velocity (top) and the root-mean-square of downstream velocity (bottom) for selected experimental runs.
158x197mm (300 x 300 DPI)

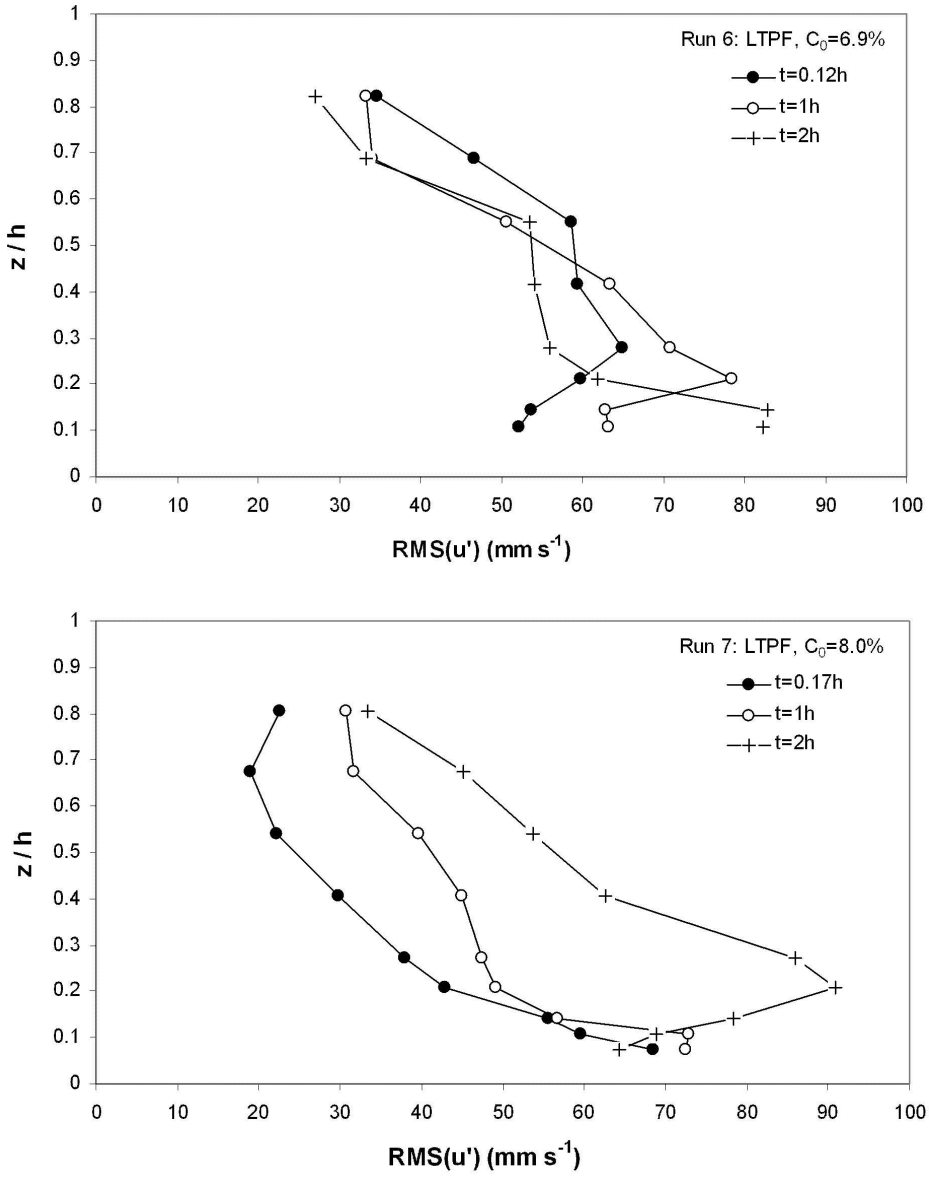


Figure 8 - Vertical profiles of the root-mean-square of downstream velocity for lower transitional plug flows. Note that RMS(u')-values change with time.
159x201mm (300 x 300 DPI)

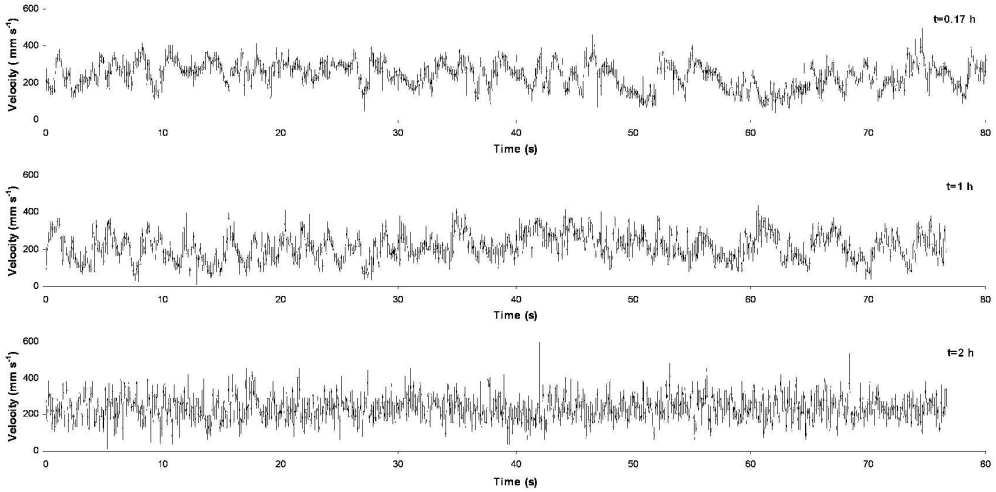


Figure 9 – Time series of downstream velocity at ~6 mm above the bed in Run 7 (C0=8.0%) at 3 different points in time. Note the pronounced saw-tooth shaped velocity fluctuations at t=0.17 h, and to a lesser degree at t=1 h
291x145mm (300 x 300 DPI)

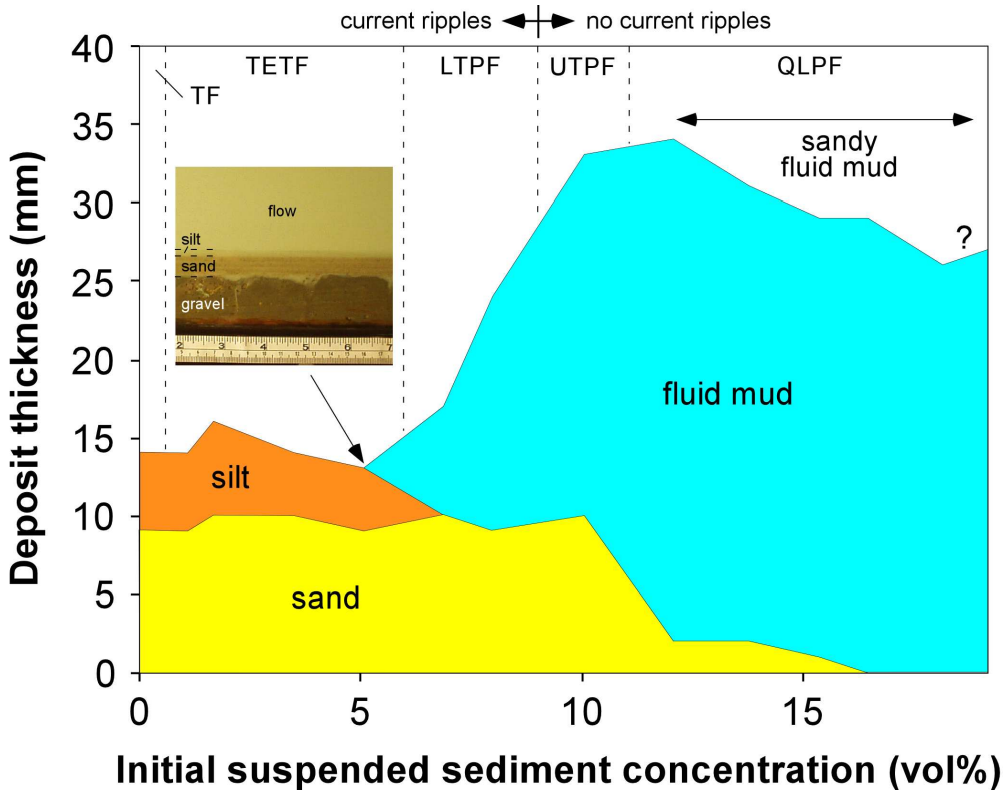


Figure 10 – Thickness and textural features of deposits formed after rapid flow deceleration and just before bedform development commenced. The question mark denotes estimated thickness, because of difficulties in recognising the flow-bed interface. Scale on photograph is in inches (top) and centimetres (bottom). The information above the graph refers to the boundary concentration for bedform development that occurred after the formation of the initial flat bed.
177x139mm (300 x 300 DPI)

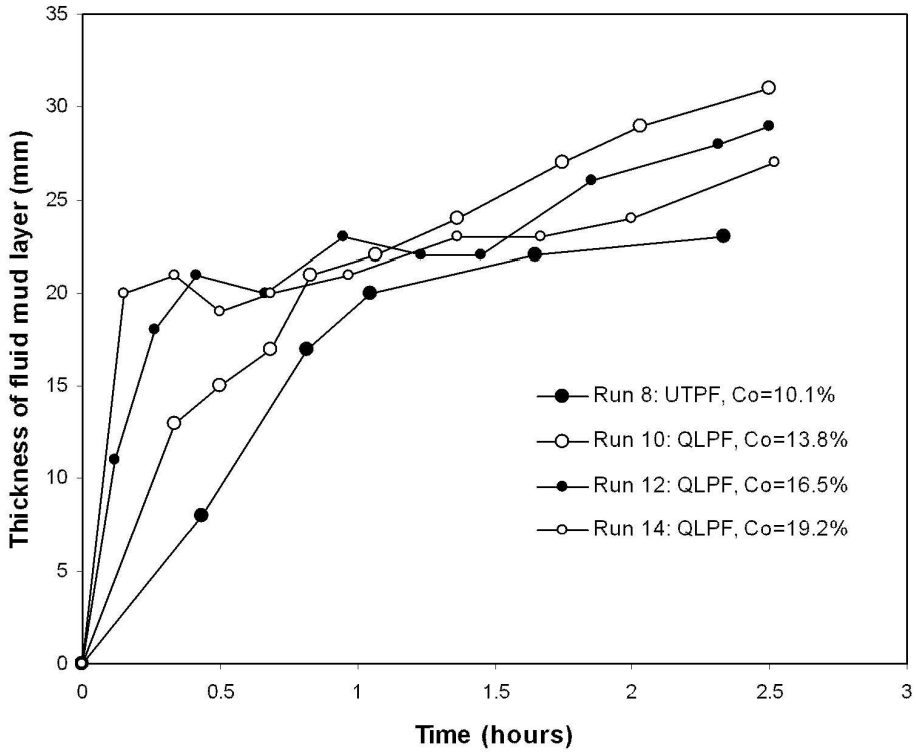


Figure 11 – Temporal development of fluid mud layer thickness in the upper transitional plug flow and the quasi-laminar plug flows.
139x114mm (300 x 300 DPI)

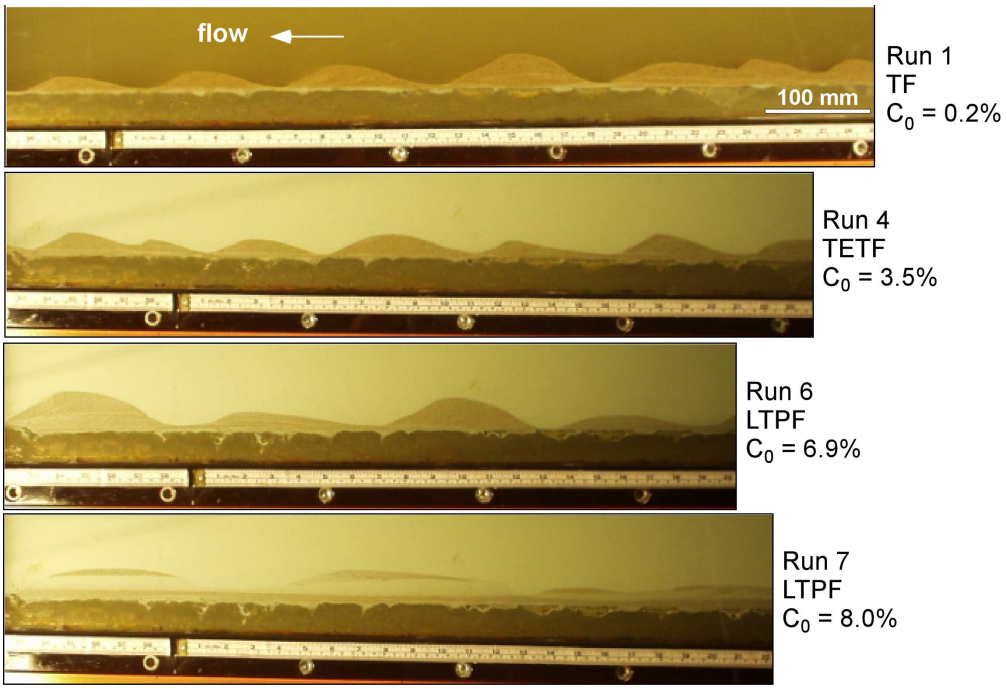


Figure 12 – Sidewall photographs of final bedforms in selected experimental runs. Note the increase in ripple height and wavelength with increasing suspended sediment concentration and the muddy character of the ripple cores in Run 7 (C0=8.0%, shown by light colours).
193x153mm (300 x 300 DPI)

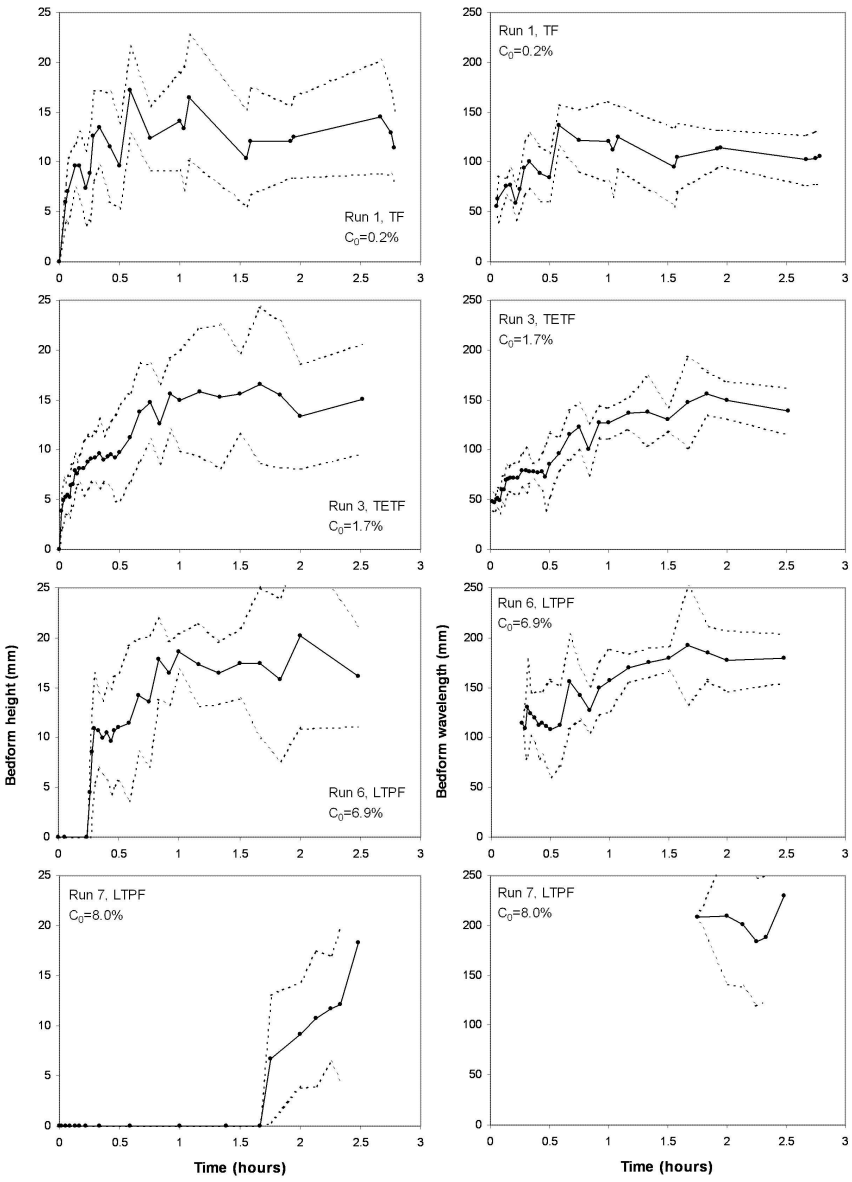


Figure 13 – Bedform height and wavelength development curves for selected runs in one turbulent flow and three lower transitional plug flows. Dashed lines indicate one standard deviation around the mean.
210x288mm (300 x 300 DPI)

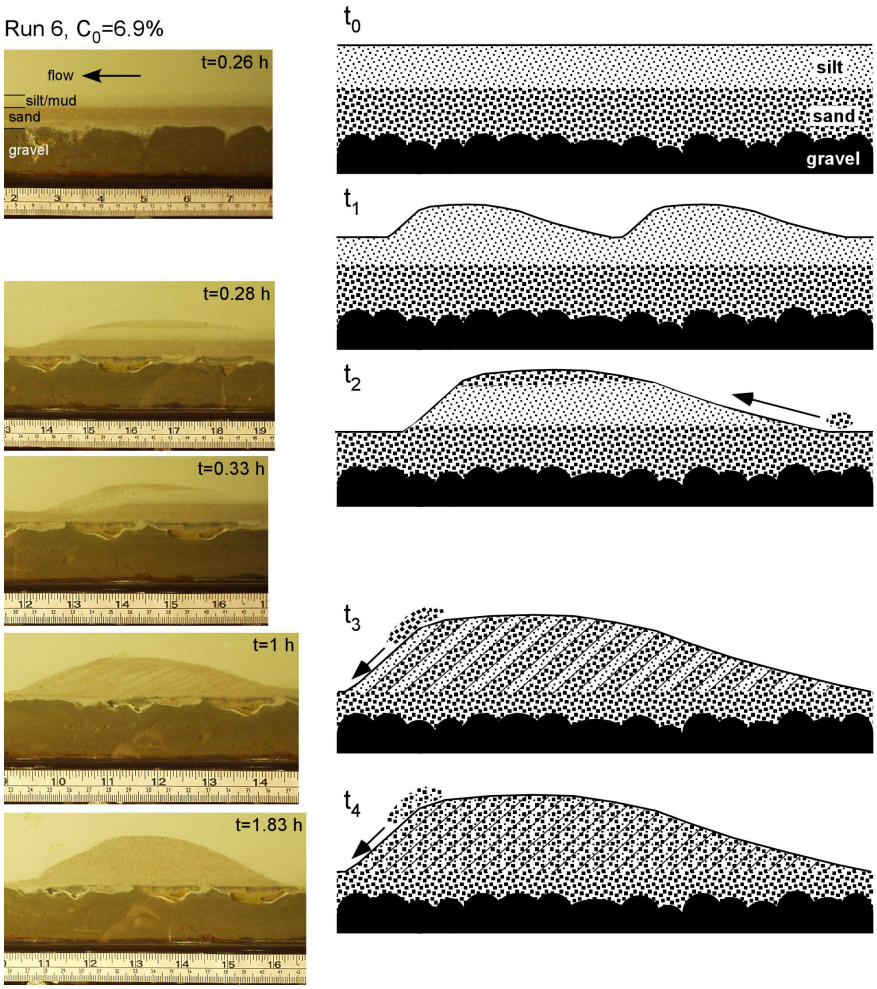


Figure 14 – Photographs and schematic drawings of bedforms in progressive stages of development starting from an initial flat bed. The drawings are valid for TF, TETF and LTPF. The photographs are from Run 6 (C0=6.9%), in which the fine-grained top of the initial flat bed (at t=0.26 h) was more cohesive than in runs with lower suspended clay concentrations. Scale on photographs is in inches (top) and centimetres (bottom).
191x188mm (300 x 300 DPI)

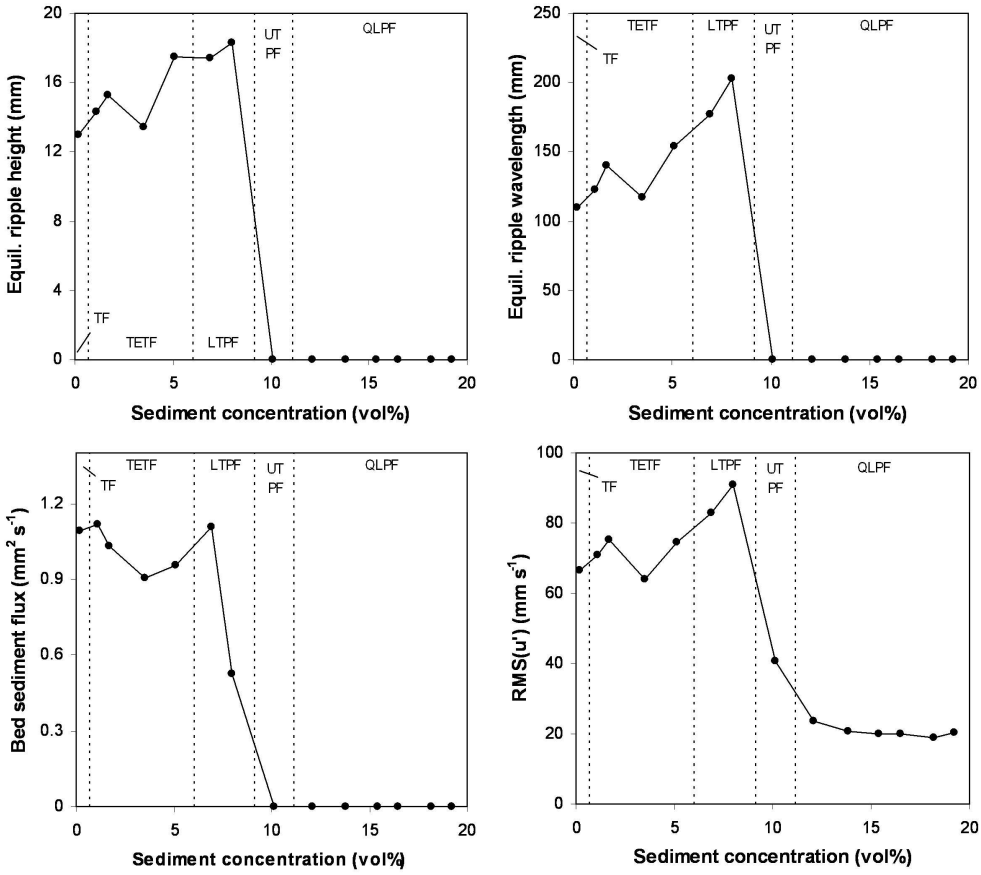


Figure 15 - Relationships between initial suspended sediment concentration and (a) equilibrium bedform height, (b) equilibrium bedform wavelength, (c) bed sediment flux and (d) RMS(u'). 201x179mm (300 x 300 DPI)

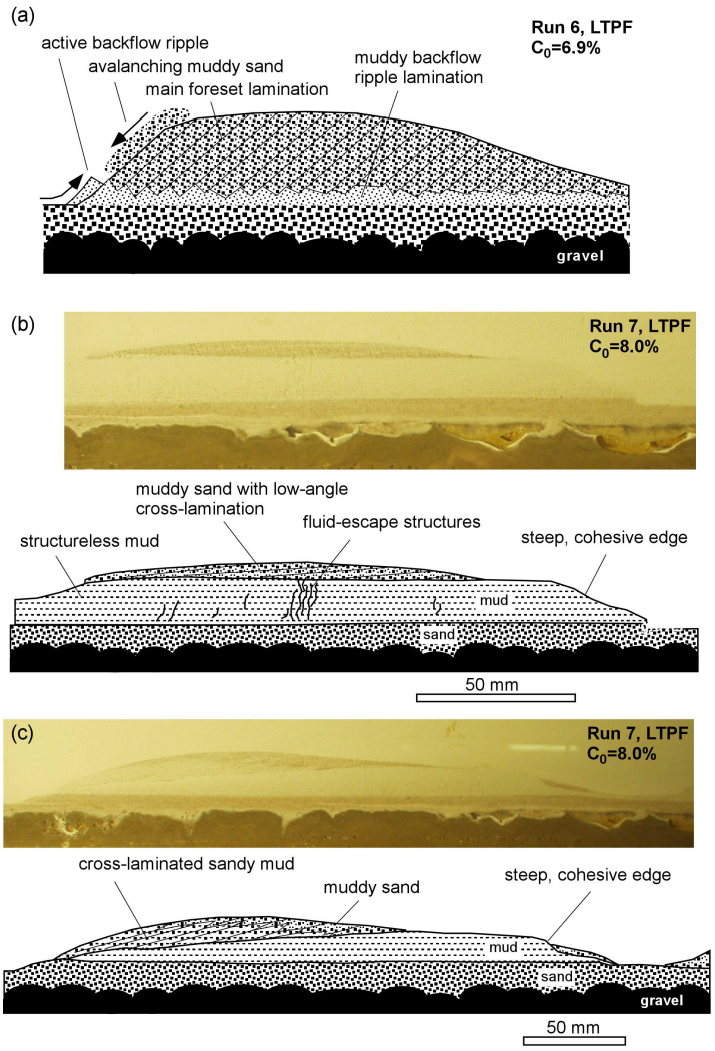


Figure 16 – (a) Schematic drawing of a current ripple with prominent backflow ripples in Run 6 (C0=6.9%). This ripple corresponds to the bedform at t4 in Fig. 14. Not to scale. (b) Photograph and labelled drawing of characteristic bedforms in Run 7 (C0=8.0%) at t=1.08 h. (c) Photograph and labelled drawing of characteristic bedforms in Run 7 at t=1.5 h. Note that the core of firm mud in (b) and (c) affects bedform properties. See text for details.
240x250mm (300 x 300 DPI)

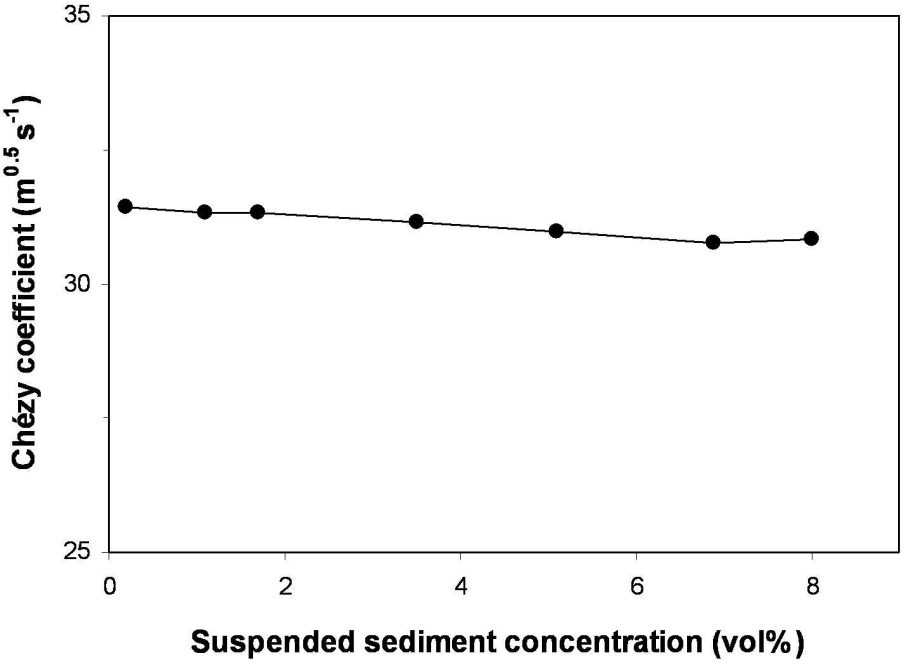


Figure 17 – Relationship between initial suspended sediment concentration and Chézy coefficient calculated for the experimental bedform heights and wavelengths.
133x99mm (300 x 300 DPI)

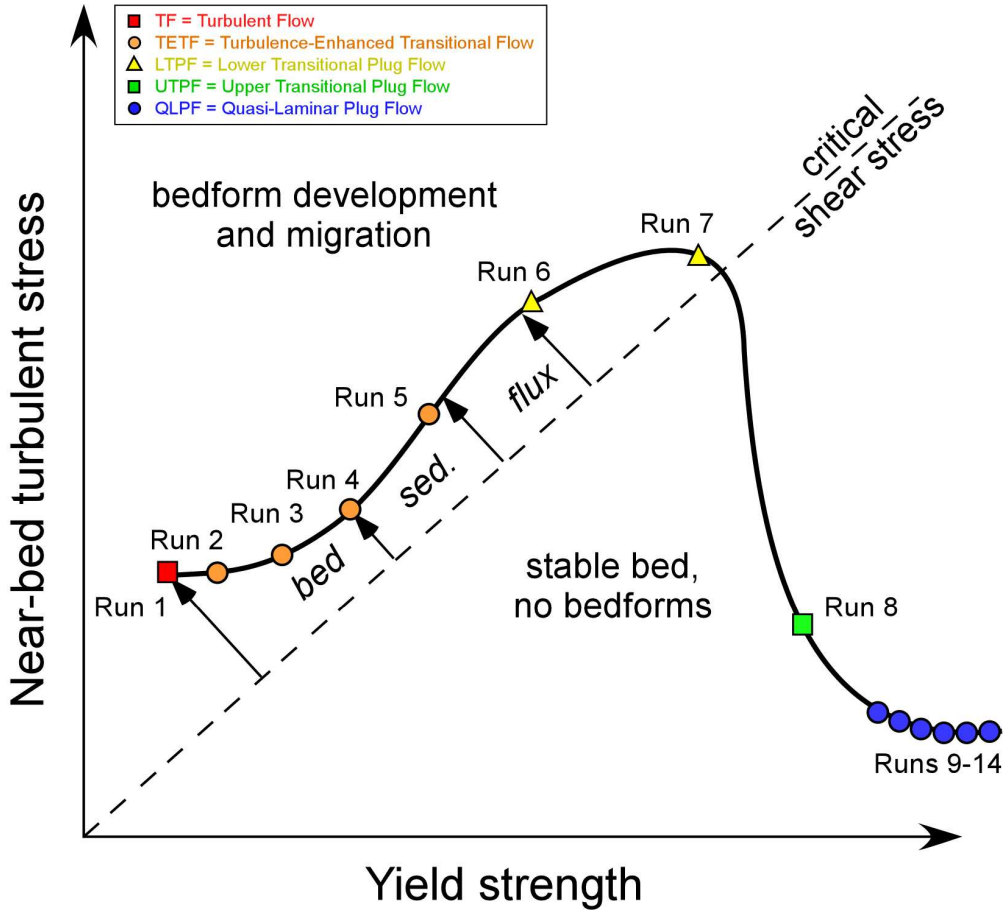


Figure 18 – Conceptual model explaining variations in bed sediment flux as function of yield strength and near-bed turbulent stress. The length of the arrows to the left and above the critical shear stress line is a measure of the bed sediment flux.
139x125mm (300 x 300 DPI)

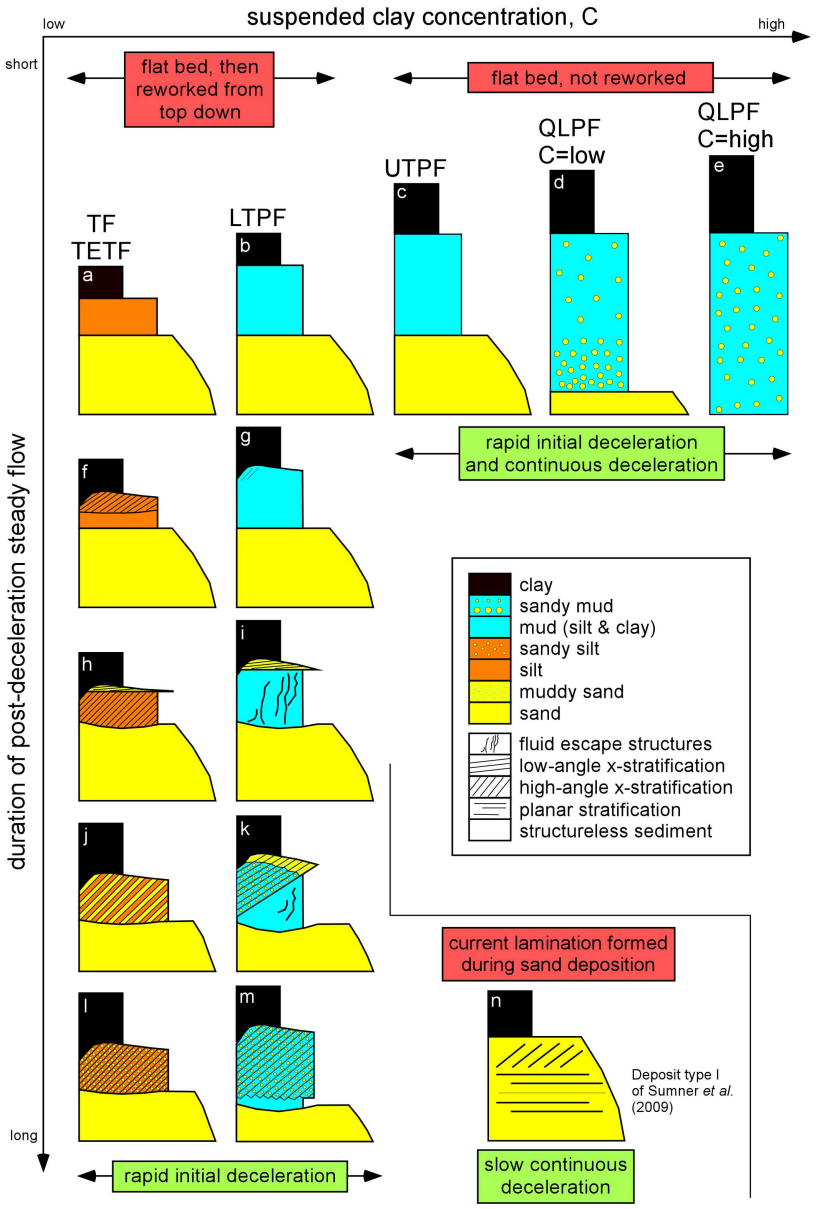


Figure 19 – Schematic sedimentary logs of mixed sand-mud facies produced by decelerated high-density flows, organised according to initial suspended sediment concentrations, duration of post-deceleration steady flow, and deceleration rate. Text in red boxes summarises principal facies types (flat, stratified, structureless) and formation mechanism. Text in green boxes summarises possible types of deceleration. See main text for details. C = concentration.
178x263mm (300 x 300 DPI)

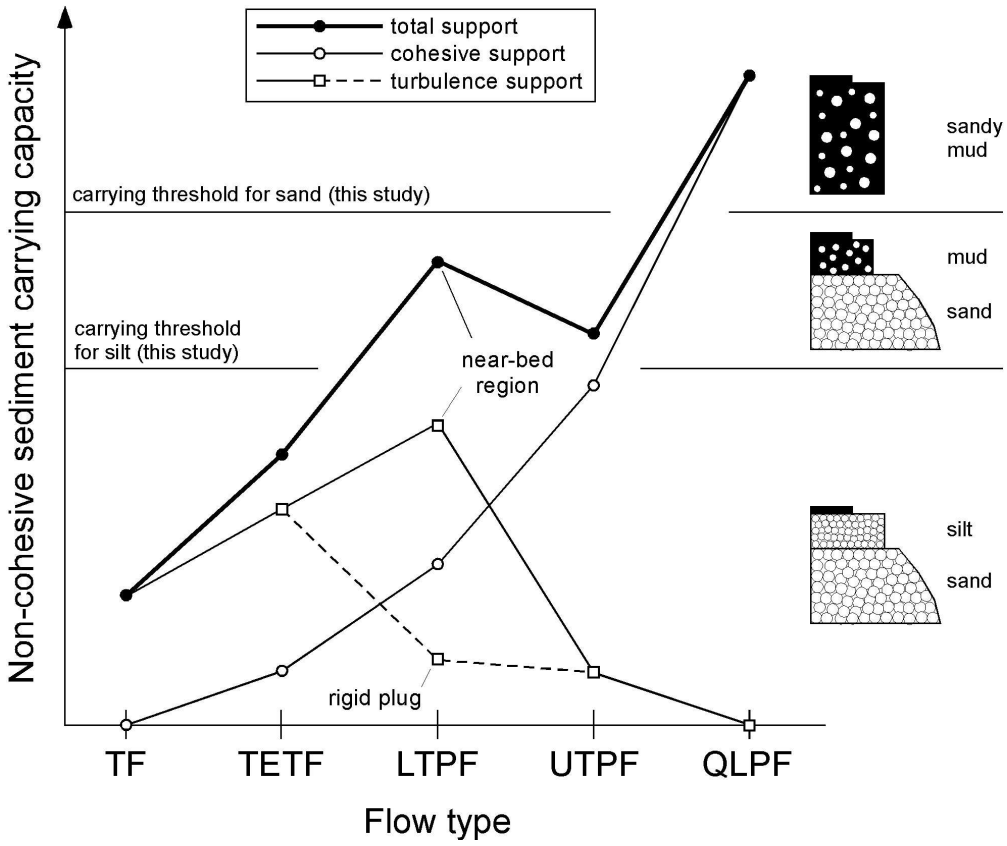


Figure 20 – Conceptual model for segregation and mixing of particle size fractions in mixed cohesive sediment flows and their sedimentary facies, based on the inferred turbulent and cohesive carrying capacity of flows with different suspended clay concentration. Total grain support (thick line) is assumed to be equal to the sum of turbulence support and cohesive support (thin lines). Turbulence support for LTPF is subdivided into the part close to the bed (thin solid black line) and the part in the overlying rigid plug (thin dashed black line); see Fig. 2.
167x140mm (300 x 300 DPI)

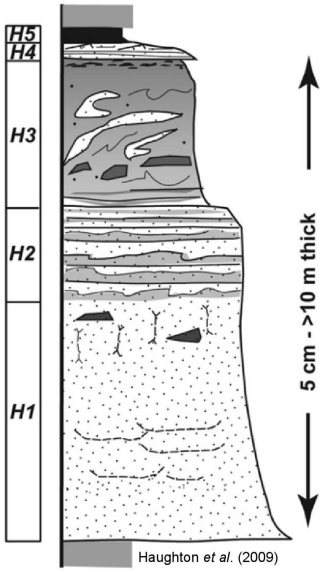


| INTERPRETATION (Haughton *et al.*, 2009) | INTERPRETATION (this study) |
|---|---|
| Suspension fallout, some shearing | Suspension fallout, some shearing |
| Traction by dilute turbulent wake | Traction by dilute turbulent wake (TF) |
| Cohesive debris flow, locally modified by sand injection from beneath, and partly reworked at top | Cohesive debris flow with QLPF behaviour, locally modified by sand injection from beneath, and partly reworked at top |
| Transitional flow (*sensu* Lowe & Guy, 2000) with intermittent turbulence suppression due to near-bed dispersed clay and internal shearing | Transitional flow (*sensu* Baas et al., 2009), with modulated turbulence (TETF, LTPF or UTPF), scouring and reworking the underlying sand |
| Progressive aggradation beneath a non-cohesive high-density turbidity current | Rapid aggradation from turbulent or transitional sediment gravity flow that is supersaturated with sand due to insufficient turbulence and cohesive support |

Figure 21 – Schematic log of idealised hybrid event bed with inferred processes of formation of H1-H5 divisions, based on Haughton et al. (2009) and this study. Modified after Haughton et al. (2009).
200x124mm (300 x 300 DPI)